Supporting Information

Confining Ultrasmall Au Nanoclusters in an Ionic Ir(III)-Based Cage for Selective Photoreduction

Zhuolin Shi,[a] Fengyang Yu,[b] Jinguo Wu,[a] Yongai Yu*,[a] Hanshu Li,[a] Xing Zhao,[a] Rong Zhang,[a] Wenjing Jiang,[c] Yiwei Liu,[a] Jianwei Wei,[d] Xuezhao Li*,[a] and Cheng He[a]

a Central Hospital of Dalian University of Technology, School of Chemistry, School of Chemical Engineering, Dalian University of Technology, Dalian 116024, China;
E-mail: xuezhaoli@dlut.edu.cn; yuyongai@dlut.edu.cn

b College of Chemistry, Xinjiang University, Xinjiang, 830046, China.

c Fujian Science & Technology Innovation Laboratory for Optoelectronic Information of China, Fuzhou, Fujian 350108, China.

d Hebei Technology Innovation Center for Energy Conversion Materials and Devices, College of Chemistry and Materials Science, Hebei Normal University, Shijiazhuang 050024, China.

Table of Contents

Section 1. Instruments

Starting materials, reagents, and solvents were purchased from commercial vendors and used as received, unless otherwise noted. All organic solvents were dried and distilled over an appropriate drying agent under an argon atmosphere.

Column chromatography was performed over silica gel (100-200 mesh or 200-300 mesh). ^{1}H, ^{13}C and 2D NMR spectra were recorded on a Bruker Advance 400 MHz spectrometer. The chemical shifts are listed in ppm on the δ scale and coupling constants were recorded in Hz. The following abbreviations were used to identify signal multiplicities: s, singlet; d, doublet; t, triplet; b, broad peaks; m, multiplet or overlapping peaks. ^{1}H assignments were made using 2D NMR methods (COSY, NOESY, HSQC, HMBC).

High-resolution quadrupole time-of-flight mass spectrometry (HR-Q-TOF-MS) was carried out on a Q-TOF MS spectrometer (Synapt G2-Si HDMS) using methanol as mobile phase.

The luminescent spectra and the decay spectra were measured with Edinburgh Instruments (FLS-1000) under anaerobic conditions. The photoluminescence decay spectra were measured with Edinburgh Instruments FLS-1000 instrument under anaerobic conditions. The photoluminescence quantum yields (Φ_{PL}) of the samples were measured on C13534 UV-NIR absolute PL Quantum Yield Spectrometer under anaerobic conditions.

UV-vis spectra were measured on a HP 8453 spectrometer.

X-ray photoelectron spectroscopy (XPS) was measured on a Near Ambient Pressure XPS system (SPECS Surface Nano Analysis GmbH, Proven-X NAP). In-situ illumination was conducted under a Xenon lamp (300 W) for 1 h. The obtained data were analyzed using XPSPEAK software with Shirley background subtraction and Gaussian-Lorentzian peak fitting, the C peak at 284.5 eV was used as a reference to correct for charging effects.

Zeta potential analysis was measured on Zetasizer Nano ZS90. Prior to the measurement, the samples were dispersed in water solutions using ultrasonic treatment to achieve a uniform dispersion.

The transmission electron microscopy (TEM) and Energy Dispersive Spectrometer (EDS) mapping were performed on Field Emission Transmission Electron Microscope (JEM-F200). The spherical aberration corrected Transmission Electron Microscopes (ACTEM) were carried out on Thermo Fisher Scientific Instruments (themis Z).

Powder X-ray diffraction (PXRD) tests were performed on SmartLab 9kw X-ray diffractometer instrument with a Cu sealed tube.

Inductively coupled plasma-optical emission spectrometry (ICP-OES) analyses were performed on PerkinElmer Avio 220.

Circular dichroism (CD) measurements were carried out on a JASCO J-810 spectrometer.

Circularly Polarized Luminescence (CPL) was carried out using a JASCO CPL-300 spectrometer under anaerobic conditions.

The light source used in catalysis measurement is 450 nm LED, which were purchased from the

Beijing China Education Au-light Co., Ltd.

In situ DRIFTS was performed on a Bruker Vertex 70v spectrometer equipped with an MCT detector at a resolution of 4 cm^{-1} with 128 scans. Sample was placed in a Harrick cell with CaF_2 windows.

Electrochemical tests were performed on CHI 760E Electrochemical Workstation under anaerobic conditions.

Section 2. Experimental Details

2.1 UV-vis and Fluorescence Measurements

The samples (1.0×10^{-5} M) in DMSO were taken at UV-vis measurements. The fluorescence spectra and photoluminescence quantum yields (Φ_{PL}) experiments were carried out using the samples (1.0×10^{-5} M) in DMSO under anaerobic conditions. The photoluminescence decay experiments were obtained with a 405 nm laser with samples (1.0×10^{-5} M) in DMSO under anaerobic conditions.

2.2 High-angle annular dark-field scanning transmission electronmicroscopy (HAADF-STEM)

HAADF-STEM samples were first dispersed in water and ultrasonicated to form a uniform suspension. A small amount of the suspension was then drop-cast onto carbon-coated copper grids and dried under ambient conditions prior to imaging.

2.3 General procedure for photoreduction of nitrobenzenes

The photocatalytic reduction of **NB**s was carried out in a 10 mL quartz tube reactor at room temperature under an argon atmosphere. Typically, as-prepared catalysts (1 mol%) was added into the reactor with a reactant mixture consisted of **NB** (0.1 mmol), NaOH (0.3 M), isopropyl alcohol (IPA, 2 mL). The system was purged with argon by bubbling through a fine-point needle for 15 min to remove dissolved oxygen. The tube was then sealed with a rubber septum to maintain an inert atmosphere. The reaction was conducted under 450 nm LED irradiation with continuous magnetic stirring. Upon completion, the reaction mixture was analyzed by ^{1}H NMR spectroscopy. For recyclability tests, the catalyst was recovered after each cycle by centrifugation, washed three times with IPA, and reused directly in subsequent cycles without further treatment.

2.4 Dynamic tracking experiments

The in situ dynamic tracking experiments were conducted with **NB** and **AOB** as substrates, respectively. Aliquots were withdrawn at designated time intervals as the reaction proceeded, and the concentration changes of reactants and products were monitored using ^{1}H NMR spectroscopy.

2.5 Binding affinities experiments

Binding affinities between Au@Δ_2R_6-**Ha** and substrates were evaluated by luminescence

quenching experiments. Au@Δ_2R_6-**Ha** (1.0×10^{-5} M, in IPA) was titrated with increasing amounts of substrate under anaerobic conditions. The emission spectra were recorded upon excitation at 405 nm. The quenching behavior was analyzed by fitting the titration curves to determine binding parameters.

(1) For the nonlinear fitting of the host-guest binding system:[S1]

$$H + G \rightleftharpoons HG$$

Here, H was the host (Au@Δ_2R_6-**Ha**), G was the guest (substrates) and HG was the complex.

$[HG] = K_a[H][G] = K_a([H]_0 - [HG])([G]_0 - [HG])$

Here, K_a was the association constant of the system, [H] was the concentration of the host, [G] was the concentration of the guest and [HG] was the concentration of the complex.

$[HG]^2 - ([H]_0 + [G]_0 + \frac{1}{K_a})[HG] + [H]_0[G]_0 = 0$

Solution of quadratic equation of one variable:

$$[HG] = \frac{\left([H]_0 + [G]_0 + \frac{1}{K_a}\right) - \sqrt{\left([H]_0 + [G]_0 + \frac{1}{K_a}\right)^2 - 4[H]_0[G]_0}}{2}$$

As in fluorescence spectra, each detection signal:

$y = a[HG] + b[H] + c[G] = (a - b - c)[HG] + b[H]_0 + c[G]_0$

Here, a, b and c are the constant.

$$y = (a - b - c)\frac{([H]_0 + [G]_0 + \frac{1}{K_a}) - \sqrt{([H]_0 + [G]_0 + \frac{1}{K_a})^2 - 4[H]_0[G]_0}}{2} + b^{[H]_0} + c^{[G]_0}$$

y and $[G]_0$ could be fitted with this equation.

Alternatively, under most conditions, the guest does not respond at the detection signal, the equation could be simplified as:

$y = a[HG] + b[H] = (a - b)[HG] + b^{[H]_0}$

$$y = (a - b)\frac{([H]_0 + [G]_0 + \frac{1}{K_a}) - \sqrt{([H]_0 + [G]_0 + \frac{1}{K_a})^2 - 4[H]_0[G]_0}}{2} + b^{[H]_0}$$

Let $k = (a - b)$, $y_0 = b^{[H]_0}$

$$y = k\frac{([H]_0 + [G]_0 + \frac{1}{K_a}) - \sqrt{([H]_0 + [G]_0 + \frac{1}{K_a})^2 - 4[H]_0[G]_0}}{2} + y_0$$

Here, the nonlinear fitting of y and $[G]_0$ is followed this equation.

(2) Stern-Volmer equation:[S2]

$$\frac{F_0}{F} = 1 + K_{SV}[G]$$

Here, K_{SV} was the Stern-Volmer constants of the system, F_0 and F are the emission intensity in the absence and presence of substrate, respectively; [G] is the concentration of the substrate.

2.6 Time-dependent DRIFTS adsorption/desorption experiment

2.6.1 CO adsorption

Time-dependent DRIFTS of CO adsorption was performed on a Bruker Vertex 70v spectrometer equipped with an MCT detector (resolution: 4 cm^{-1}, 64 scans per spectrum). Approximately 20.0 mg of catalyst was evenly spread in a Harrick in situ DRIFTS cell to ensure full coverage and adequate sample height for effective gas–solid interaction.

Prior to CO dosing, high-purity argon (1200 mL h^{-1}) was passed through the cell for at least 1 h to remove residual air, moisture, and CO_2. Background spectra were collected after signal stabilization. CO gas (800 mL h^{-1}) was then introduced for 2 h, during which spectra were recorded at regular intervals to monitor adsorption. After equilibrium was reached, CO was purged with argon until no further change in peak intensity was observed, indicating complete desorption of weakly bound species. The sample was then irradiated in situ with a 450 nm LED while exposed to CO (500 mL min^{-1}) at room temperature for 15 min. Final spectra were collected after argon purging to remove residual CO.

2.6.2 Substrates adsorption/desorption

Substrate adsorption and desorption experiments were performed similarly to the CO adsorption protocol with minor modifications. A parallel U-tube was connected to the gas inlet; its outlet was packed with cotton to prevent liquid backflow. Model substrates dissolved in a CH_2Cl_2/MeOH mixture (10 mL, 1: 1 v/v) were placed at the bottom of the U-tube. Argon gas (400 mL h^{-1}) was passed through the U-tube to volatilize the substrate and deliver it into the DRIFTS cell in the vapor phase. After adsorption equilibrium was reached, desorption was monitored by purging with argon and gradually increasing the temperature to 60 °C while recording spectra to track desorption behavior.

2.7 Electrochemical measurement

All electrochemical tests were performed on CHI 660E Electrochemical Workstation with a conventional three-electrode system. Photocurrent measurements and electrochemical impedance spectroscopy (EIS) were performed with the catalyst-coated FTO as the working electrode, a platinum wire as a counter electrode and an Ag/AgCl reference electrode, in an aqueous solution of Na_2SO_4 (0.1 M). The 2 mg of catalyst was added into 0.5 mL of ethanol and 20 μL of Nafion mixed solution. Then a 100 μL suspension was dropped on the surface of the FTO glass with an area of 1.0 cm^2 and dried at room temperature for measurements. The photocurrent density was recorded after an initial equilibration period to ensure a stable baseline for comparison.

Section 3. Computational Details

3.1 DFT calculations

The geometric structures of Δ_2R_6-**Ha**, Δ_2R_6-**Hp**, Au@Δ_2R_6-**Ha**, **NB**-Au@Δ_2R_6-**Ha**, **AOB**-Au@Δ_2R_6-**Ha** and **AB**-Au@Δ_2R_6-**Ha** were optimized by density functional theory (DFT) calculations using B97D hybrid functional with D2 version of Grimme's dispersion.[S3, S4] The basis set was using LANL2DZ for Ir and Au,[S5] and 6-31G(d) for other elements.[S6] All the DFT calculations were performed using Gaussian 16 (Revision B.01) package.[S7]

3.2 Electron density distribution calculation

The electron density distribution (EDD) of the electron-hole orbitals in Au@Δ_2R_6-**H** during the $S_0 \rightarrow S_1$ transition was analyzed with Multiwfn and visualized by VMD. [S8-S11]

3.3 Adsorption energies calculations

The adsorption energies (E_{ads}) was calculated as:

$$\Delta E_{ads} = E_{ad}^{*} - E^{*} - E_{ad}$$

where E_{ad}^{*} is the total energy of system, E^{*} and E_{ad} are the energies of the substrate Au@Δ_2R_6-**Ha** structure and the adsorbed substrates, respectively.

Section 4. Synthetic Procedures and Characterization

All reactions were performed under Ar atmosphere and using dry solvents unless otherwise stated.

4.1 Synthesis and characterization of Δ_2R_6-Hp

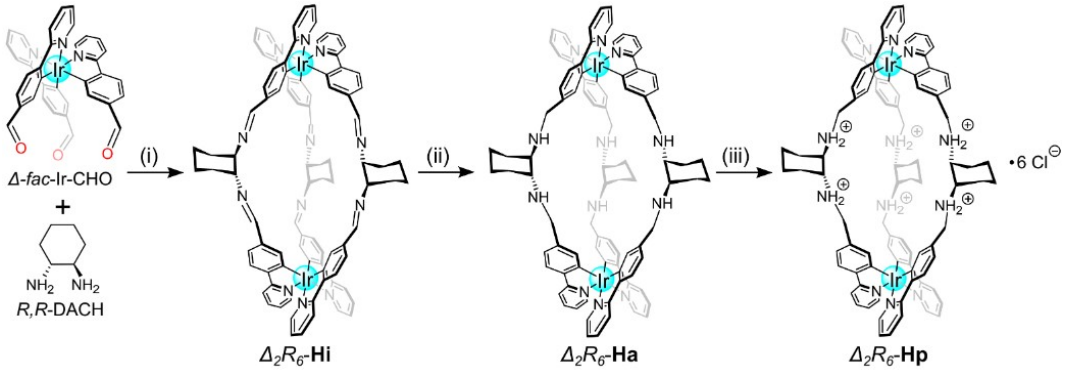

Scheme S1 Synthesis of enantiomeric Δ_2R_6-**Hp**. Reaction conditions: (i) p-Toluenesulfonic acid (TsOH), CH_3CN, Toluene, 110 °C, 12 h, 90% in total; (ii) $NaBH_4$, MeOH, CH_2Cl_2, room temperature, 12 h, 93%; (iii) HCl 0.1 M, MeOH, room temperature, 98%.

4.1.1 Synthesis of Δ_2R_6-Hi

The cyclometalate ligands *Δ-fac*-Ir-CHO and the corresponding assembly Δ_2R_6-**Hi** were synthesized according to our reported procedures. [S12]

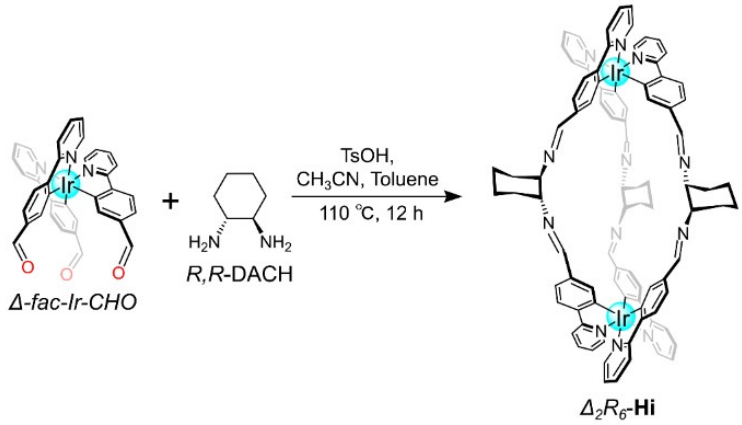

Scheme S2 Synthesis route of Δ_2R_6-**Hi**.

In detail, *Δ-fac*-Ir-CHO (37 mg, 0.05 mmol), *R,R*-DACH (8.8 mg, 0.075 mmol) and p-Toluene sulfonic acid (TsOH) (2.6 mg, 0.015 mmol) was dissolved in a mix solvent of acetonitrile (10 mL) and toluene (20 mL). The mixture was stirred at 110 °C for 12 h under argon. After cooling to room temperature, the solvent was removed under vacuum and the solid was dissolved in CH_2Cl_2. Diethyl ether was diffused into CH_2Cl_2 solution and got the orange crystals. The crystals were washed with diethyl ether, and afforded Δ_2R_6-**Hi** after drying in 90 % yield (38 mg).

HR-Q-TOF-MS: *m/z* $[M + H]^+$ calcd for $[C_{90}H_{79}Ir_2N_{12}]^+$:1712.5819, found: 1713.5775.

^{1}H NMR (500 MHz, CD_2Cl_2, ppm) δ 7.98 (s, 1H), 7.96 (s, 1H), 7.71-7.67 (m, 2H), 7.63 (dd, J =

1.5 Hz, J = 8.0 Hz, 1H), 7.52 (d, J = 5.0 Hz, 1H), 6.99-6.96 (m, 2H), 3.11 (s, 1H), 2.27 (m, 1H), 1.89 (m, 1H), 1.53 (m, 1H), 1.38 (d, J = 10.0 Hz).

^{13}C NMR (101 MHz, CD_2Cl_2, ppm) δ 166.3, 161.4, 160.6, 147.6, 146.3, 140.8, 137.7, 136.9, 124.5, 122.9, 119.8, 117.8, 73.1, 30.2, 21.8.

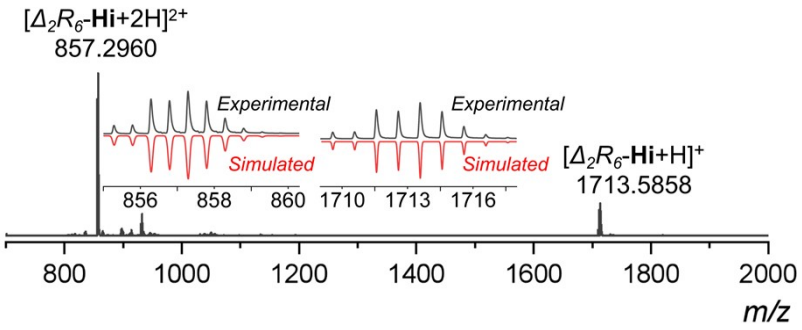

Fig. S1 HR-Q-TOF-MS spectrum of Δ_2R_6-**Hi**.

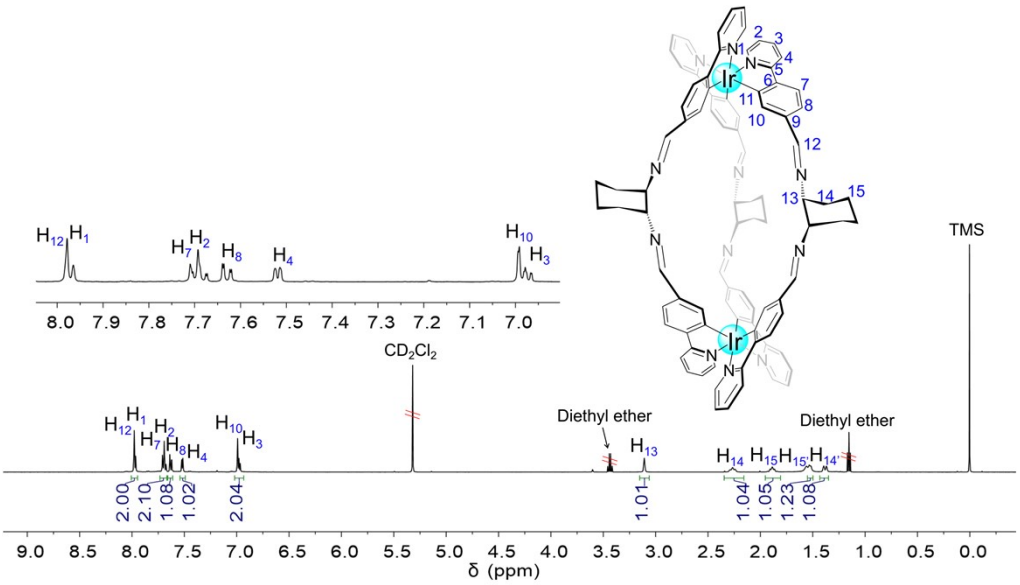

Fig. S2 ^{1}H NMR (400 MHz, CD_2Cl_2, 298 K) spectrum of Δ_2R_6-**Hi**.

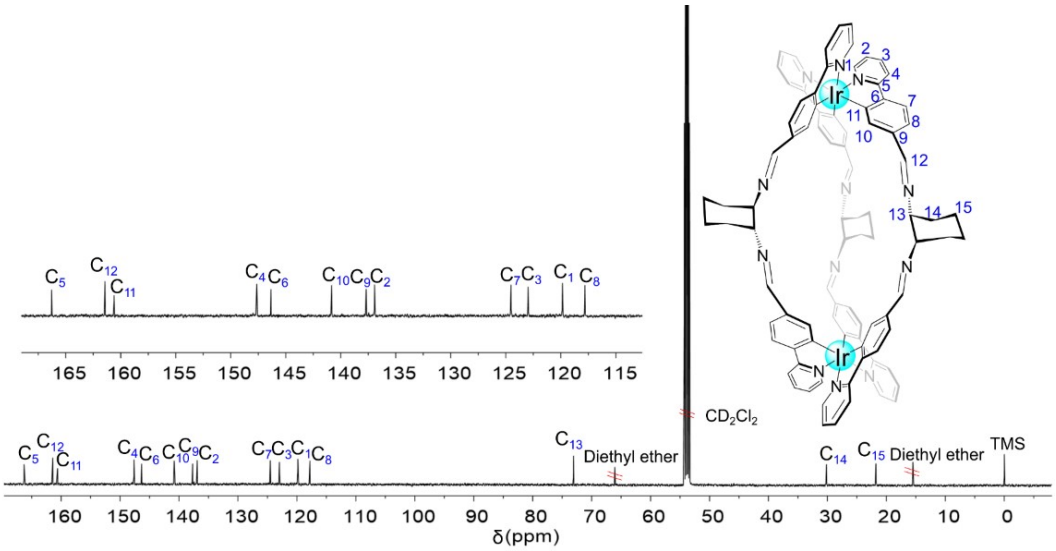

Fig. S3 ^{13}C NMR (101 MHz, CD_2Cl_2, 298 K) spectrum of Δ_2R_6-**Hi**.

4.1.2 Synthesis of Δ_2R_6-Ha

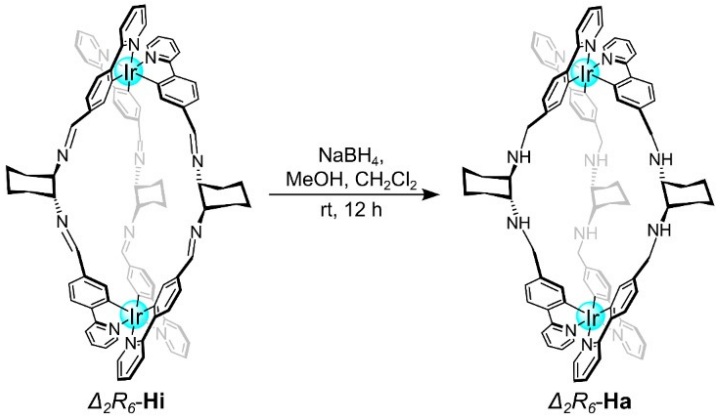

Scheme S3 Synthesis route of Δ_2R_6-**Ha**.

Δ_2R_6-**Hi** (38 mg, 0.022 mmol) was dissolved in in a mixture of methanol and dichloromethane (1: 1 v/v, 20 mL) under argon atmosphere. Following, sodium borohydride (16.5 mg, 0.48 mmol, 20 equiv.) was added in five batches at ice-water bath, and the reaction mixture was stirred at room temperature for a 12 h. Water (10 mL) was then added, and stirring was continued for an additional 2 h. The reaction mixture was extracted with CH_2Cl_2, and the organic layer was evaporated to yield a light yellow solid. The crude product was washed with diethyl ether and dried under vacuum to afford the product in 93% yield (35 mg).

HR-Q-TOF-MS: *m/z* $[M + 2H]^{2+}$calcd for $[C_{90}H_{92}Ir_2N_{12}]^{2+}$: 863.3415, found: 863.3420; $[M + 3H]^{3+}$calcd for $[C_{90}H_{93}Ir_2N_{12}]^{3+}$: 575.8968, found: 575.8972.

^{1}H NMR (400 MHz, DMSO-d_6) δ 8.07 (d, J = 8.4 Hz, 1H, H_1), 7.76 (td, J = 7.8, 1.7 Hz, 1H, H_2), 7.70 (d, J = 8.2 Hz, 1H, H_7), 7.42 (dd, J = 5.7, 1.6 Hz, 1H, H_4), 7.11 – 7.03 (m, 1H, H_3), 6.88 (d, J

= 8.0 Hz, 1H, H_8), 6.59 – 6.52 (m, 1H, H_{10}), 3.57 – 3.44 (m, 1H, H_{12}), 3.18 (d, J = 12.0 Hz, 1H, $H_{12'}$), 2.18 (s, 1H, H_{13}), 1.87 (s, 1H, H_{14}), 1.51 (d, J = 33.8 Hz, 2H, H_{15}, HN), 1.14 (d, J = 34.3 Hz, 2H, $H_{15'}$, $H_{14'}$).

^{13}C NMR (101 MHz, DMSO-d_6) δ 166.14 (C_5), 161.34 (C_9), 147.10 (C_4), 142.59 (C_6), 141.9 (C_{11}), 137.12 (C_2, C_{10}), 124.72 (C_7), 122.77 (C_3), 120.10 (C_8), 119.22 (C_1), 59.32 (C_{13}), 52.22 (C_{12}), 28.79 (C_{14}), 22.95 (C_{15}).

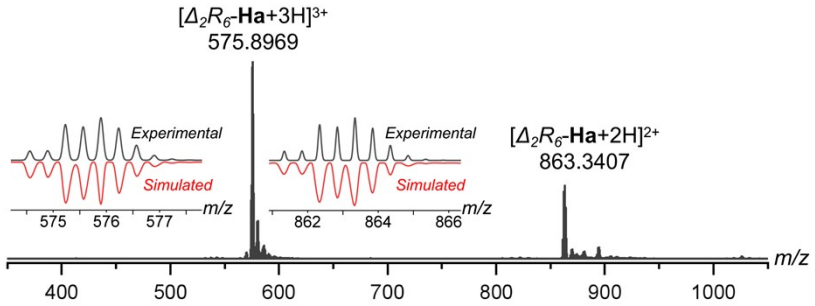

Fig. S4 HR-Q-TOF-MS spectrum of Δ_2R_6-**Ha**.

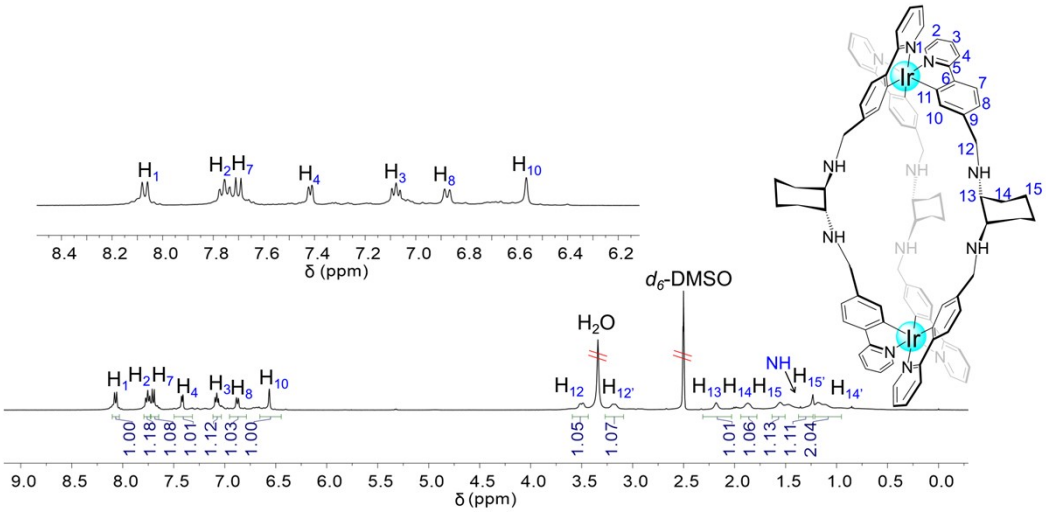

Fig. S5 ^{1}H NMR (400 MHz, DMSO-d_6, 298 K) spectrum of Δ_2R_6-**Ha**.

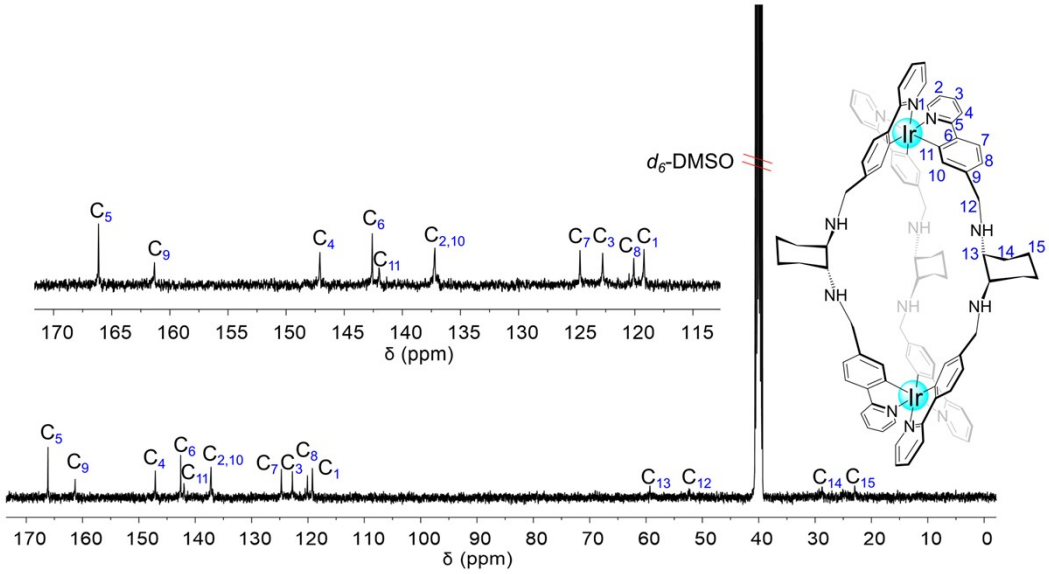

Fig. S6 ^{13}C NMR spectrum (101 MHz, DMSO-d_6, 298K) of Δ_2R_6-**Ha**.

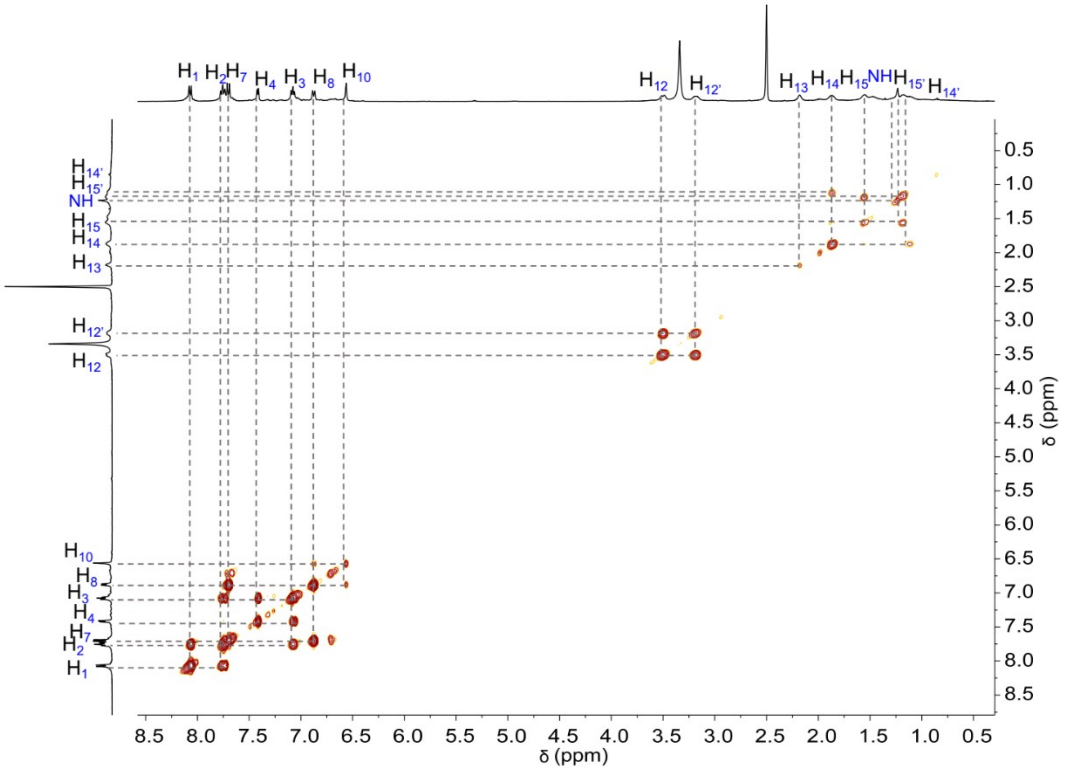

Fig. S7 ^{1}H-^{1}H COSY spectrum (400 MHz, DMSO-d_6, 298K) of Δ_2R_6-**Ha**.

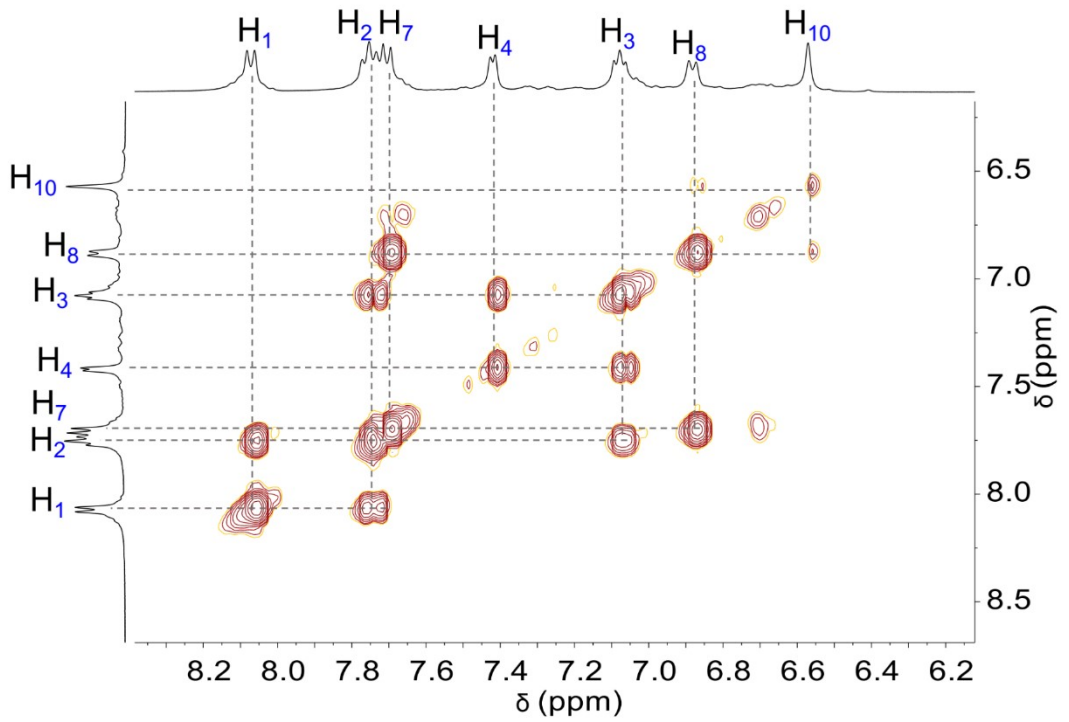

Fig. S8 Partial^{1}H-^{1}H COSY spectrum (400 MHz, DMSO-d_6, 298K) of Δ_2R_6-**Ha**.

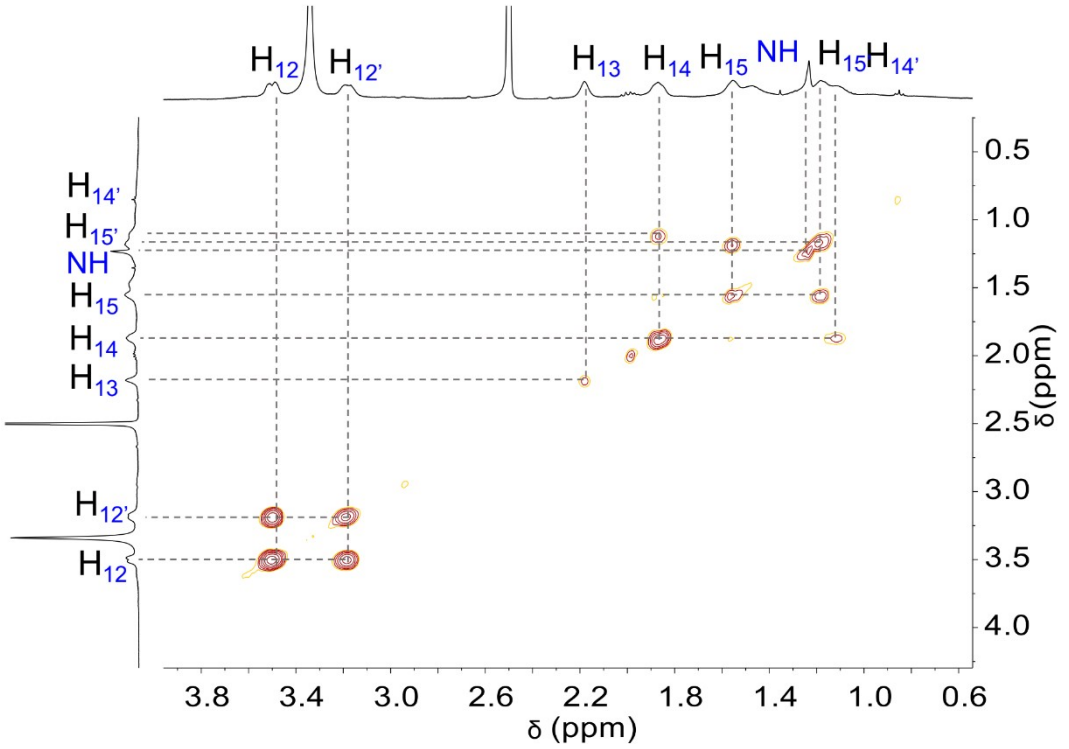

Fig. S9 Partial^{1}H-^{1}H COSY spectrum (400 MHz, DMSO-d_6, 298K) of Δ_2R_6-**Ha**.

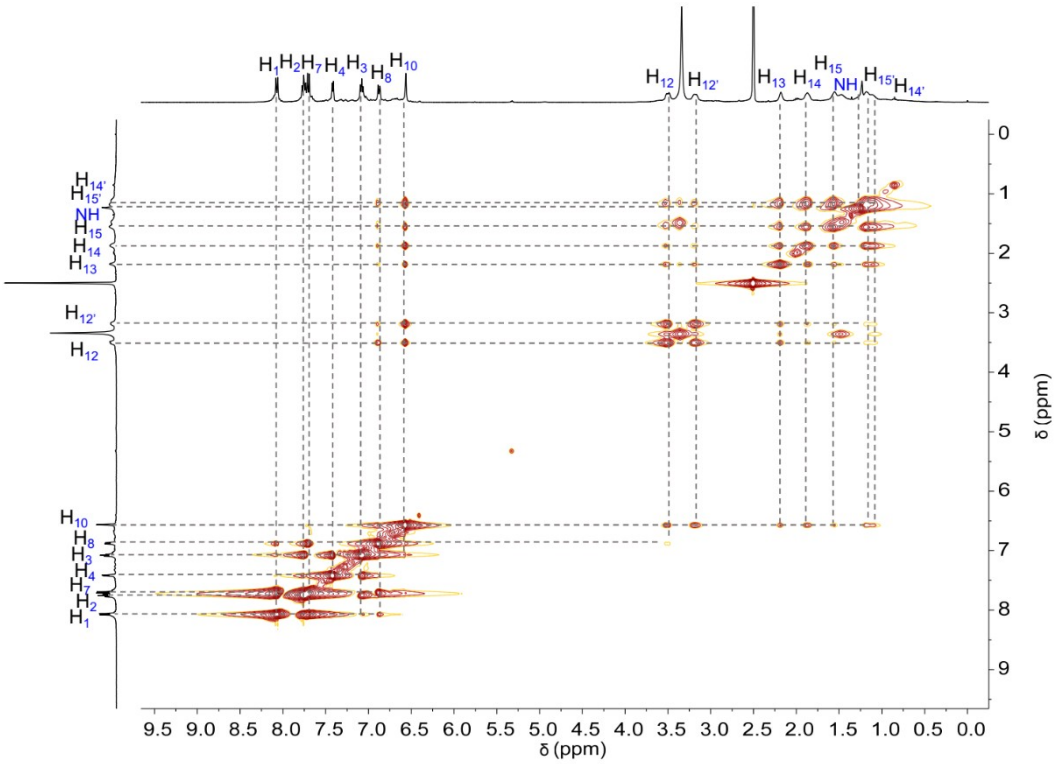

Fig. S10 ^{1}H-^{1}H NOESY spectrum (400 MHz, DMSO-d_6, 298K) of Δ_2R_6-**Ha**.

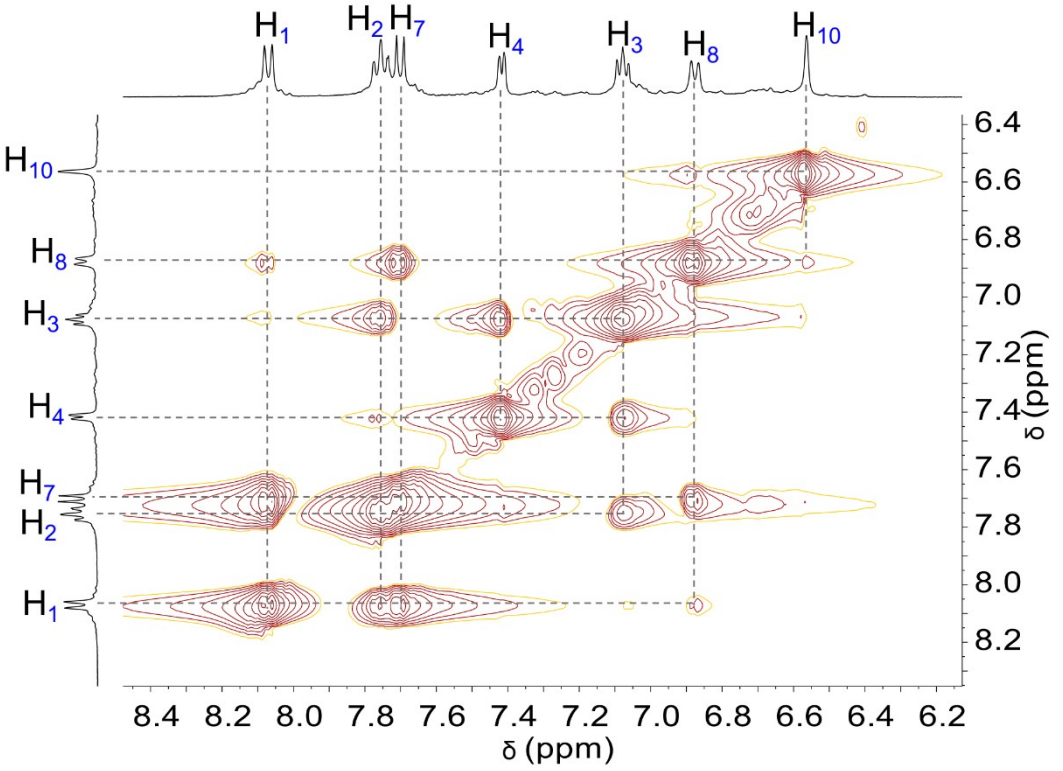

Fig. S11 Partial ^{1}H-^{1}H NOESY spectrum (400 MHz, DMSO-d_6, 298K) of Δ_2R_6-**Ha**.

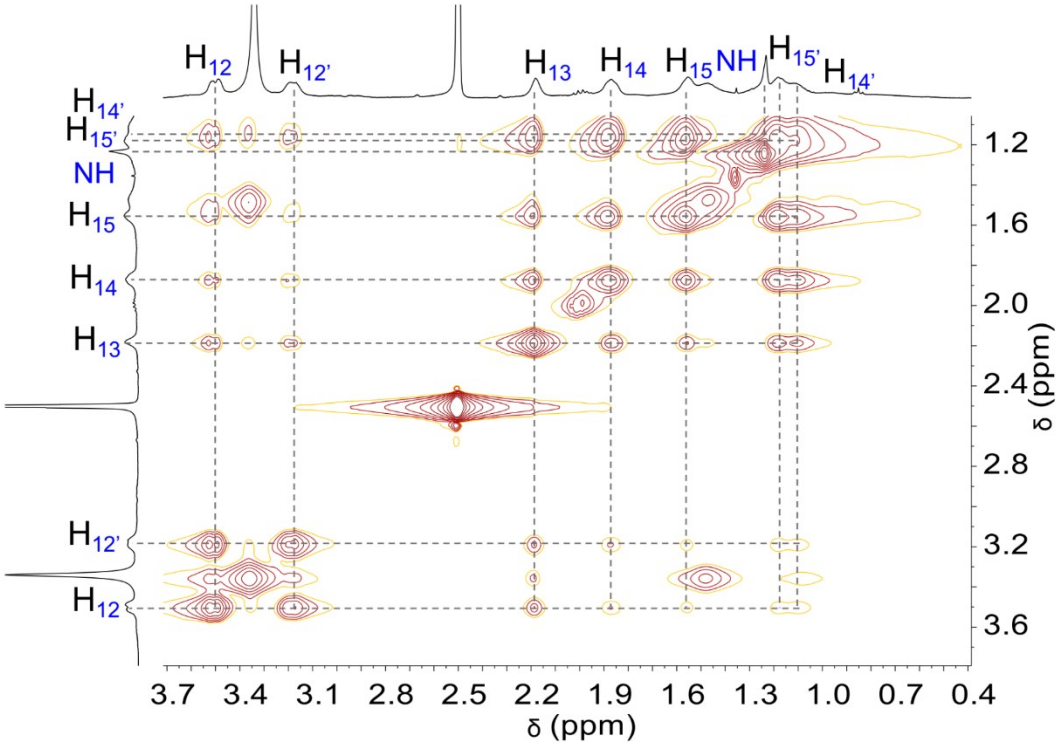

Fig. S12 Partial ^{1}H-^{1}H NOESY spectrum (400 MHz, DMSO-d_6, 298K) of Δ_2R_6-**Ha**.

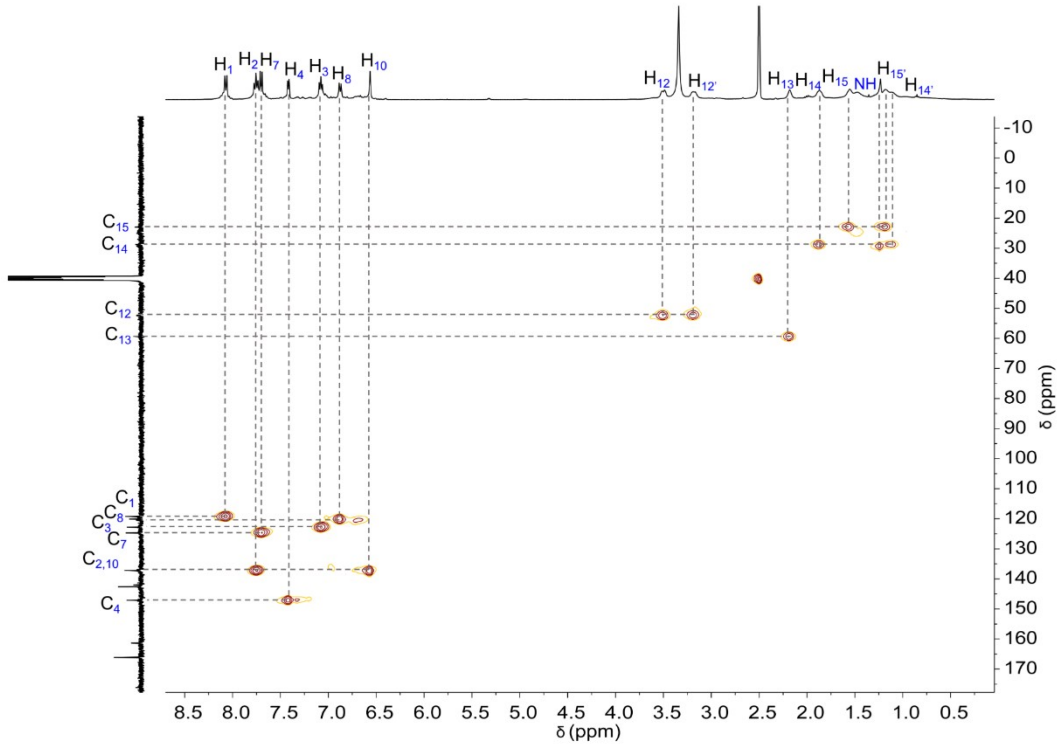

Fig. S13 ^{1}H-^{13}C HSQC spectrum (400 MHz, DMSO-d_6, 298K) of Δ_2R_6-**Ha**.

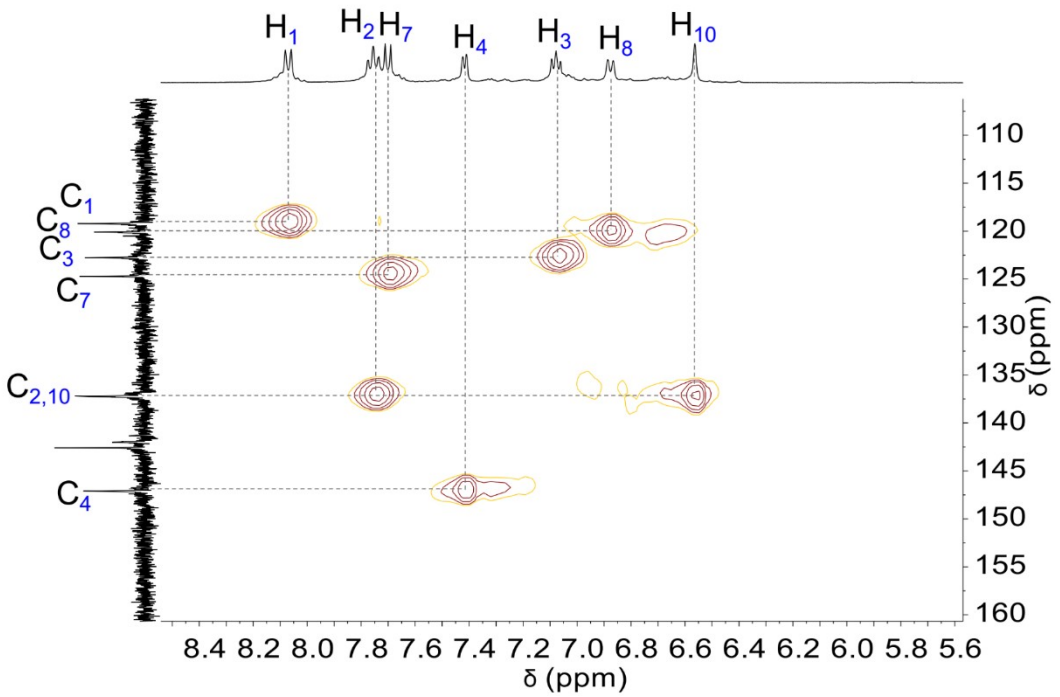

Fig. S14 Partial ^{1}H-^{13}C HSQC spectrum (400 MHz, DMSO-d_6, 298K) of Δ_2R_6-**Ha**.

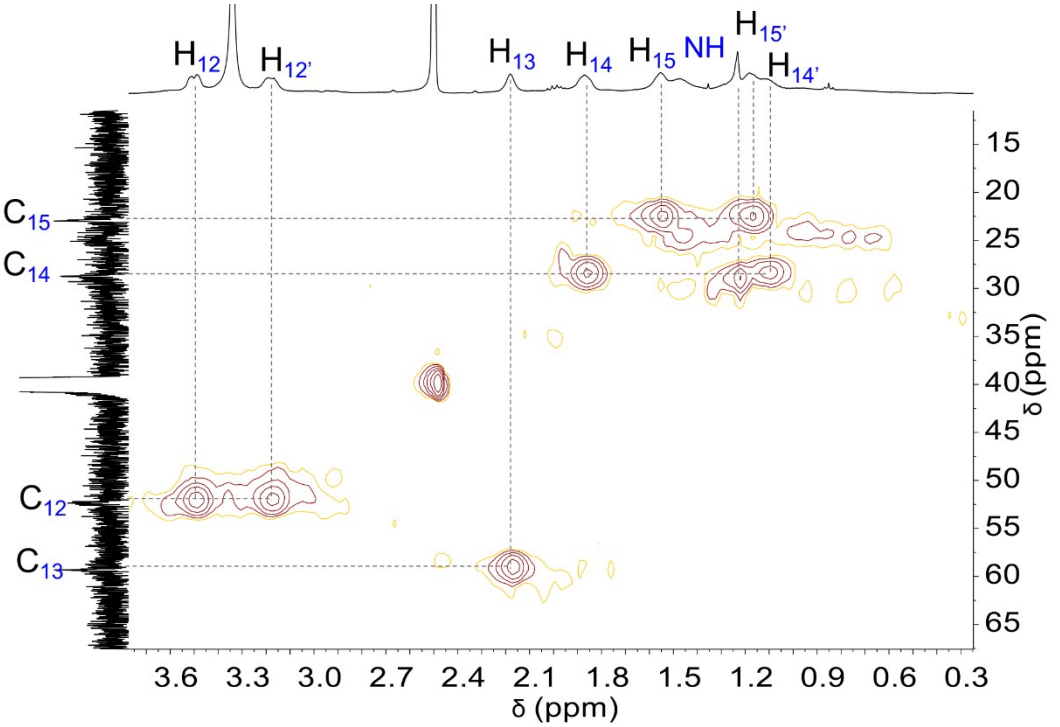

Fig. S15 Partial ^{1}H-^{13}C HSQC spectrum (400 MHz, DMSO-d_6, 298K) of Δ_2R_6-**Ha**.

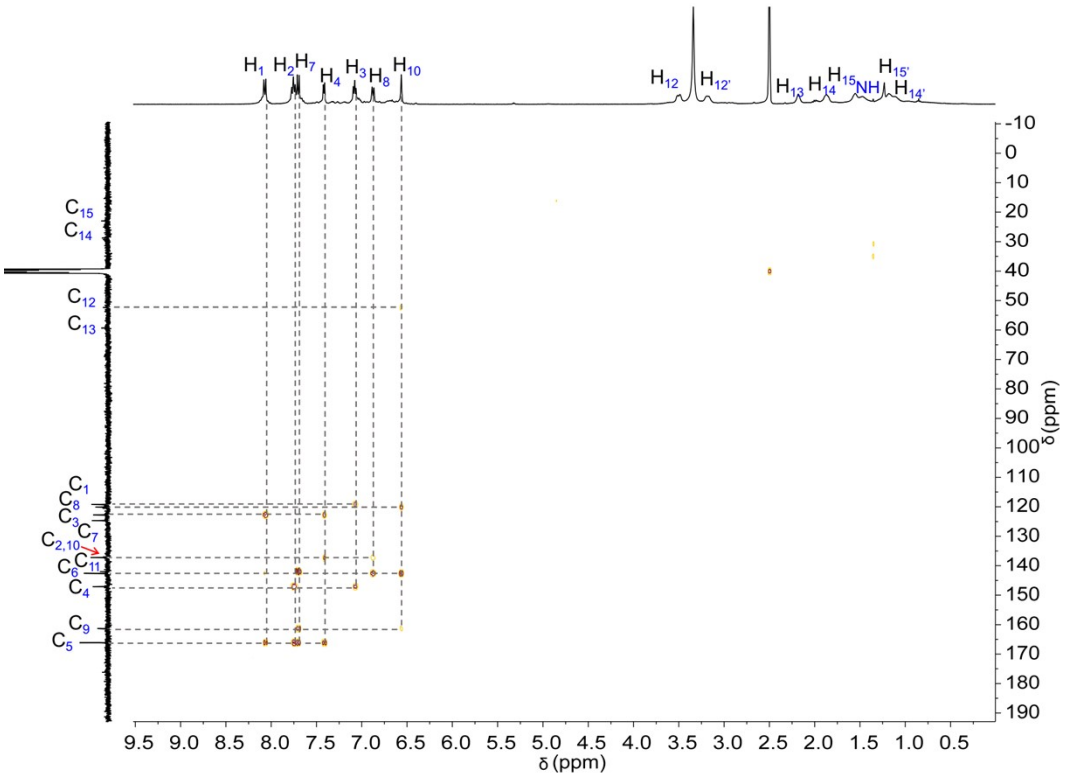

Fig. S16 ^{1}H-^{13}C HMBC spectrum (400 MHz, DMSO-d_6, 298K) of Δ_2R_6-**Ha**.

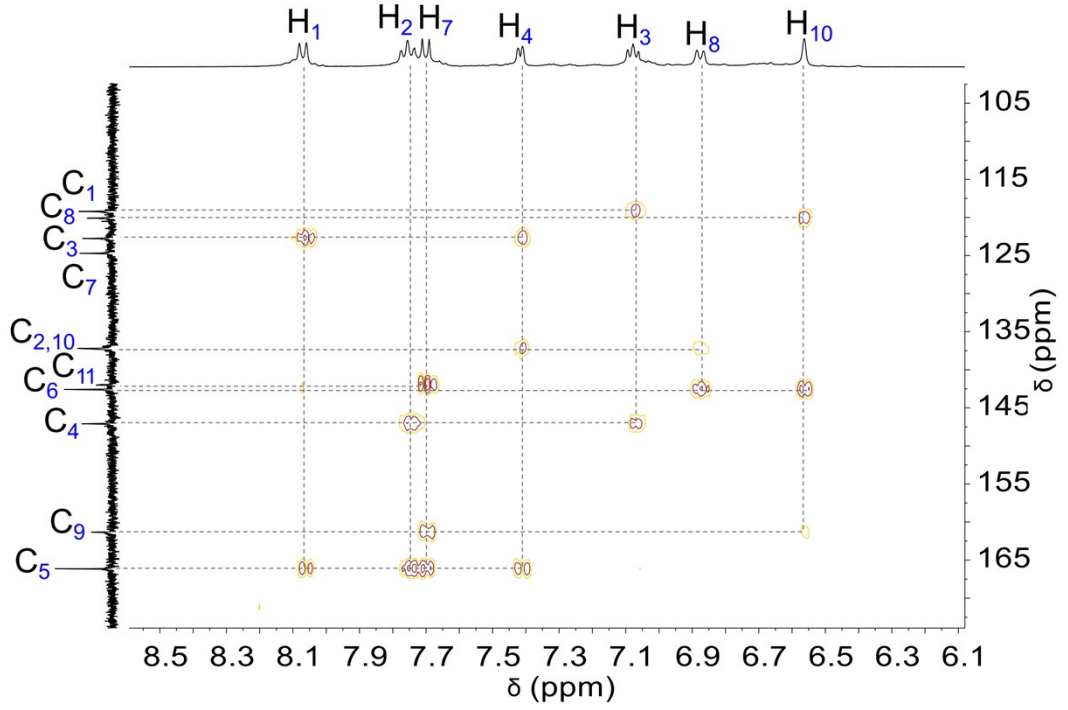

Fig. S17 Partial ^{1}H-^{13}C HMBC spectrum (400 MHz, DMSO-d_6, 298K) of Δ_2R_6-**Ha**.

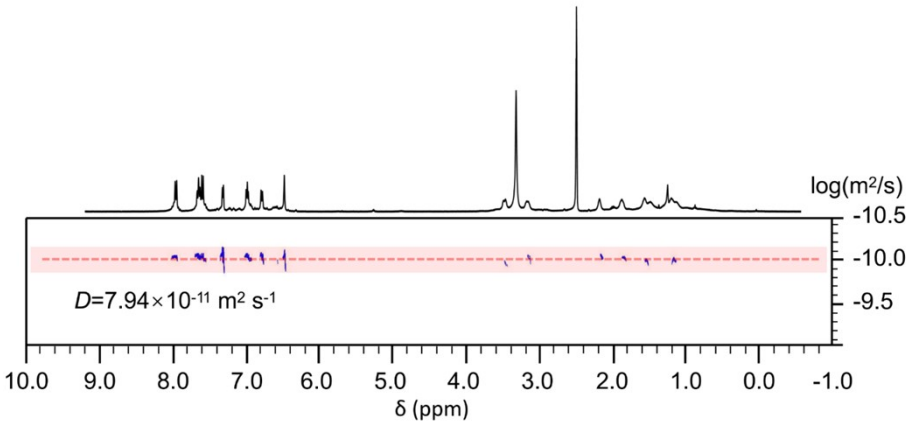

Fig. S18 ^{1}H DOSY NMR (400 MHz, DMSO-d_6, 298 K) spectrum of Δ_2R_6-**Ha**.

4.1.3 Synthesis of Δ_2R_6-Hp

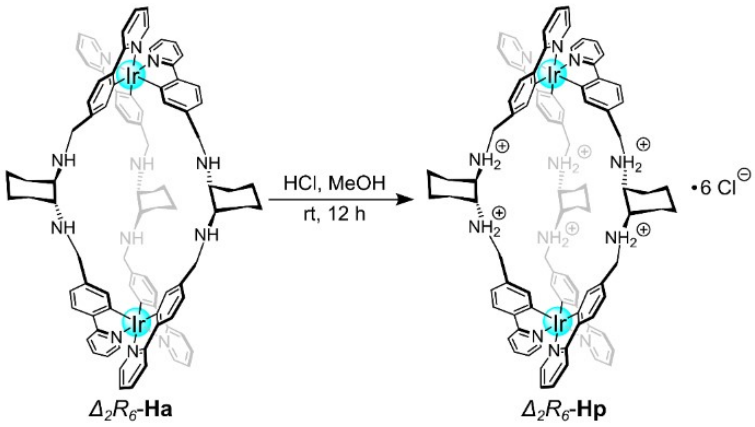

Scheme S4 Synthesis route of Δ_2R_6-**Hp**.

Δ_2R_6-**Ha** (35 mg, 0.020 mmol) was dissolved in methanol (30 mL), and HCl in ethanol (2 M, 1.8 mL) was added dropwise under vigorous stirring to adjust the pH to 2. The reaction mixture was stirred at room temperature for 12 h. After solvent evaporation, a yellowish-green solid of Δ_2R_6-**Hp** was obtained in 98% yield (38 mg).

HR-Q-TOF-MS: *m/z* $[M - 4H - 6Cl]^{2+}$calcd for $[C_{90}H_{92}Ir_2N_{12}]^{2+}$: 863.3415, found: 863.3424; $[M - 3H - 6Cl]^{3+}$calcd for $[C_{90}H_{93}Ir_2N_{12}]^{3+}$: 575.8968, found: 575.8970.

^{1}H NMR (400 MHz, D_2O): δ 8.22 (d, J = 7.7 Hz, 1H, H_1), 8.05 (d, J = 8.2 Hz, 1H, H_7), 7.85 (t, J = 7.9 Hz, 1H, H_2), 7.37 (d, J = 5.6 Hz, 1H, H_4), 7.19 (s, 1H, H_{10}), 7.12 (d, J = 8.0 Hz, 1H, H_8), 7.05 (t, J = 13.0, 11.1 Hz, 1H, H_3), 3.62 (m, 1H, H_{12}), 2.81 (d, J = 11.9 Hz, 1H, $H_{12'}$), 2.01 – 1.08 (m, J = 6.8 Hz, 5H, H_{13}, H_{15}, $H_{14'}$, H_{14}, $H_{15'}$).

^{13}C NMR (101 MHz, D_2O): δ 163.64 (C_5), 160.21 (C_9), 147.65 (C_4), 146.41 (C_6), 137.79 (C_2, C_{10}), 125.06 (C_7), 123.72 (C_3, C_8), 119.75 (C_1), 44.56 (C_{12}), 35.09 (C_{13}), 29.47 (C_{14}), 23.10 (C_{15}).

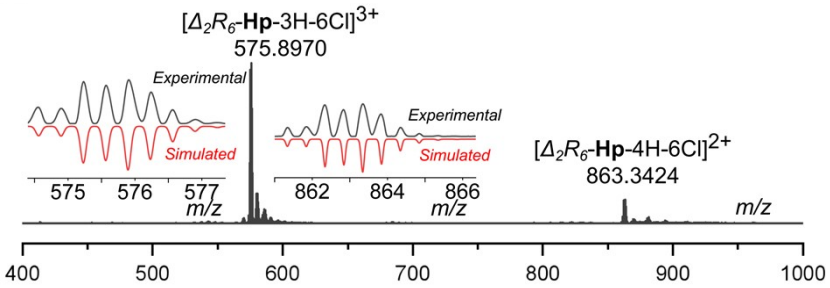

Fig. S19 HR-Q-TOF-MS spectrum of Δ_2R_6-**Hp**.

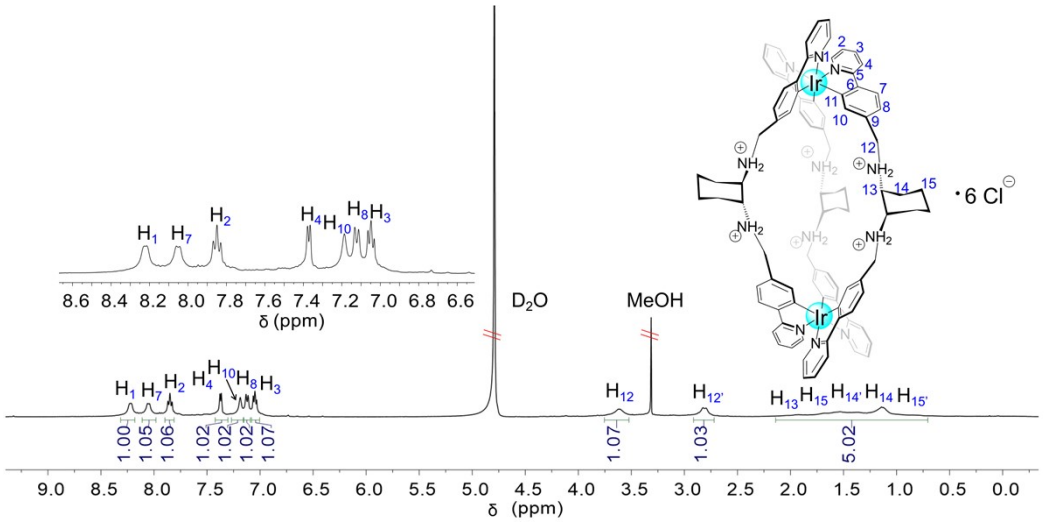

Fig. S20 ^{1}H NMR (400 MHz, D_2O, 298 K) spectrum of Δ_2R_6-**Hp**.

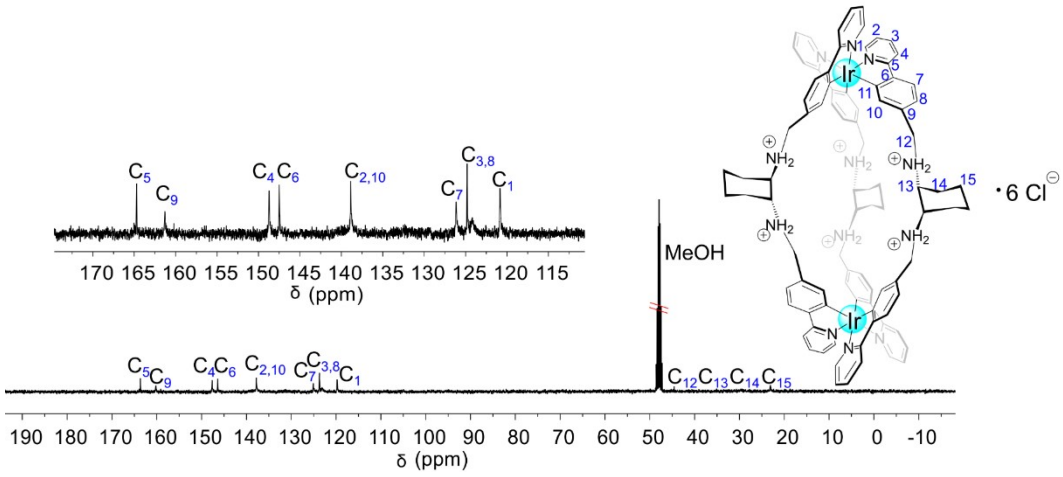

Fig. S21 ^{13}C NMR spectrum (101 MHz, D_2O, 298K) of Δ_2R_6-**Hp**.

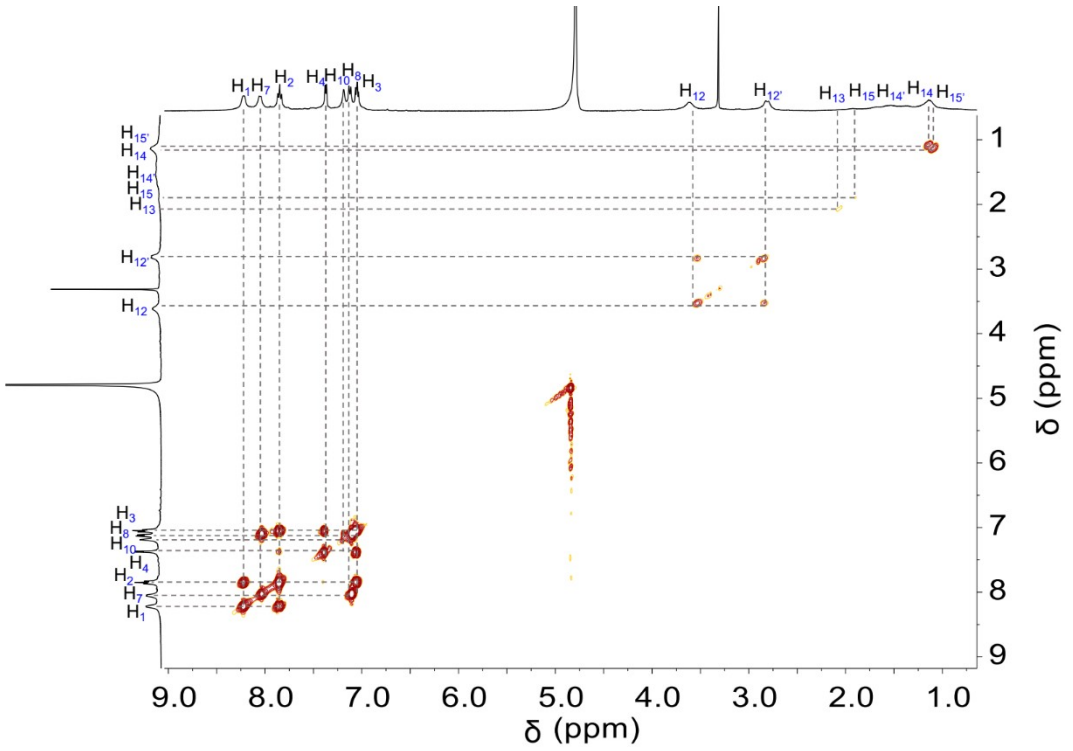

Fig. S22 ^{1}H-^{1}H COSY spectrum (400 MHz, D_2O, 298K) of Δ_2R_6-**Hp**.

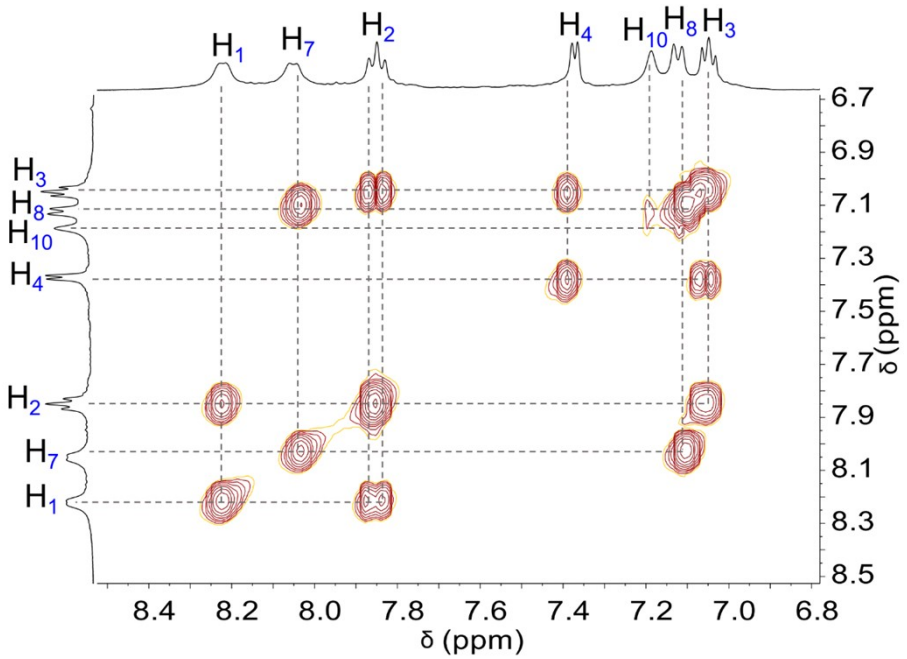

Fig. S23 Partial ^{1}H-^{1}H COSY spectrum (400 MHz, D_2O, 298K) of Δ_2R_6-**Hp**.

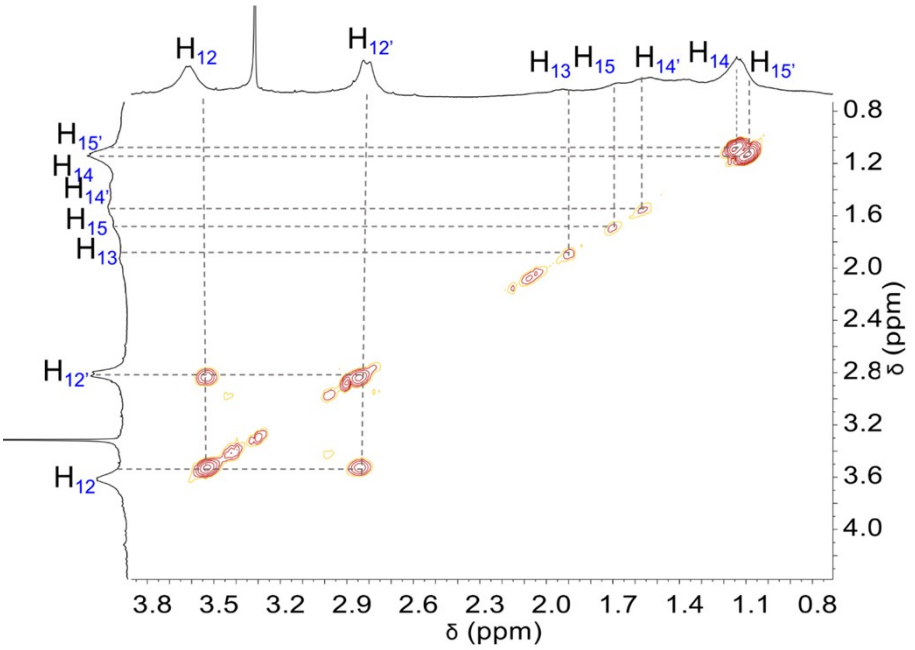

Fig. S24 Partial ^{1}H-^{1}H COSY spectrum (400 MHz, D_2O, 298K) of Δ_2R_6-**Hp**.

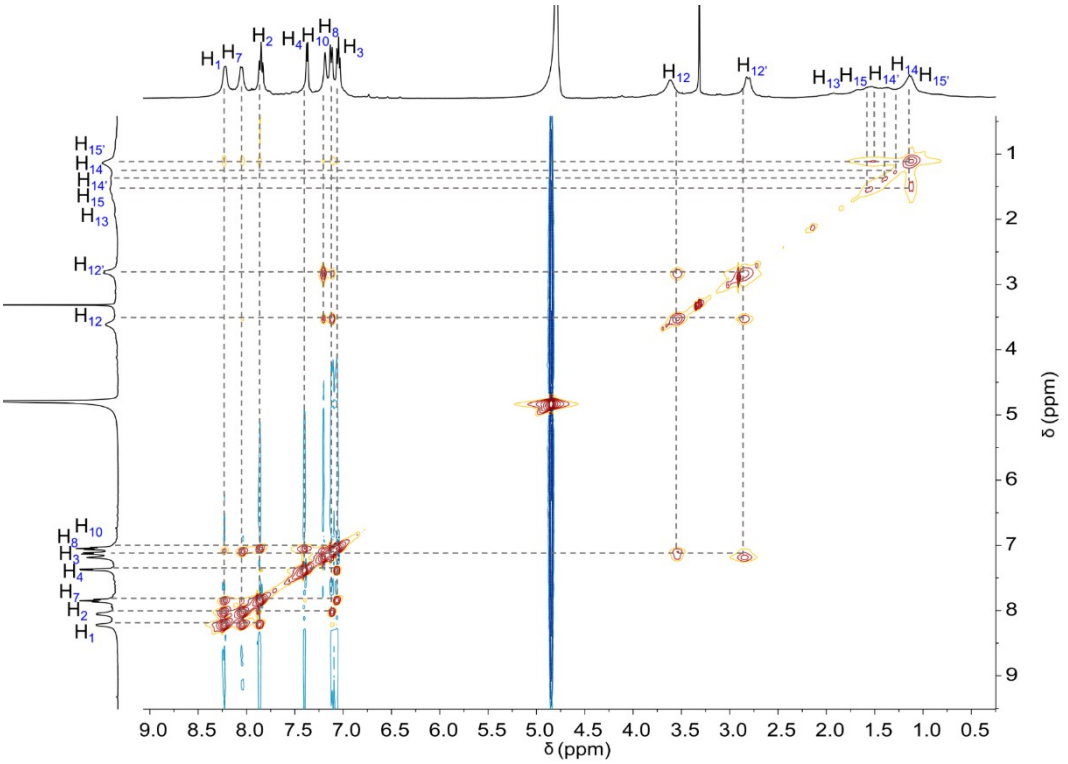

Fig. S25 ^{1}H-^{1}H NOESY spectrum (400 MHz, D_2O, 298K) of Δ_2R_6-**Hp**.

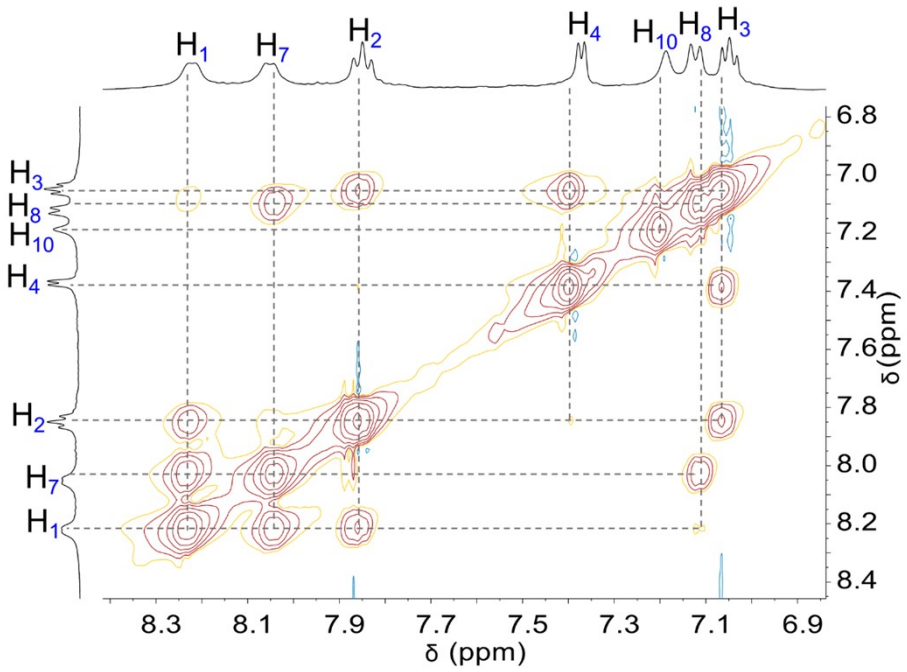

Fig. S26 Partial ^{1}H-^{1}H NOESY spectrum (400 MHz, D_2O, 298K) of Δ_2R_6-**Hp**.

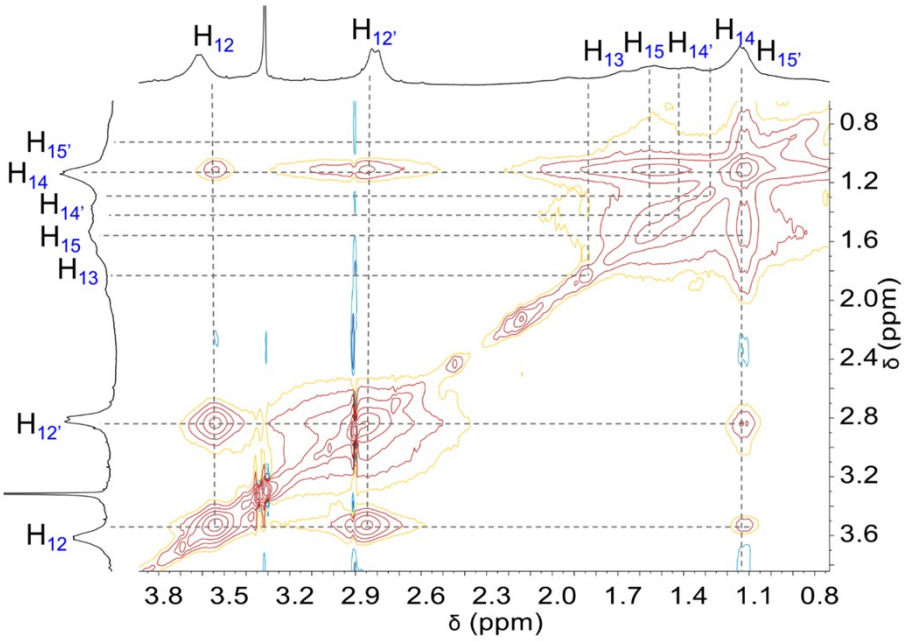

Fig. S27 Partial ^{1}H-^{1}H NOESY spectrum (400 MHz, D_2O, 298K) of Δ_2R_6-**Hp**.

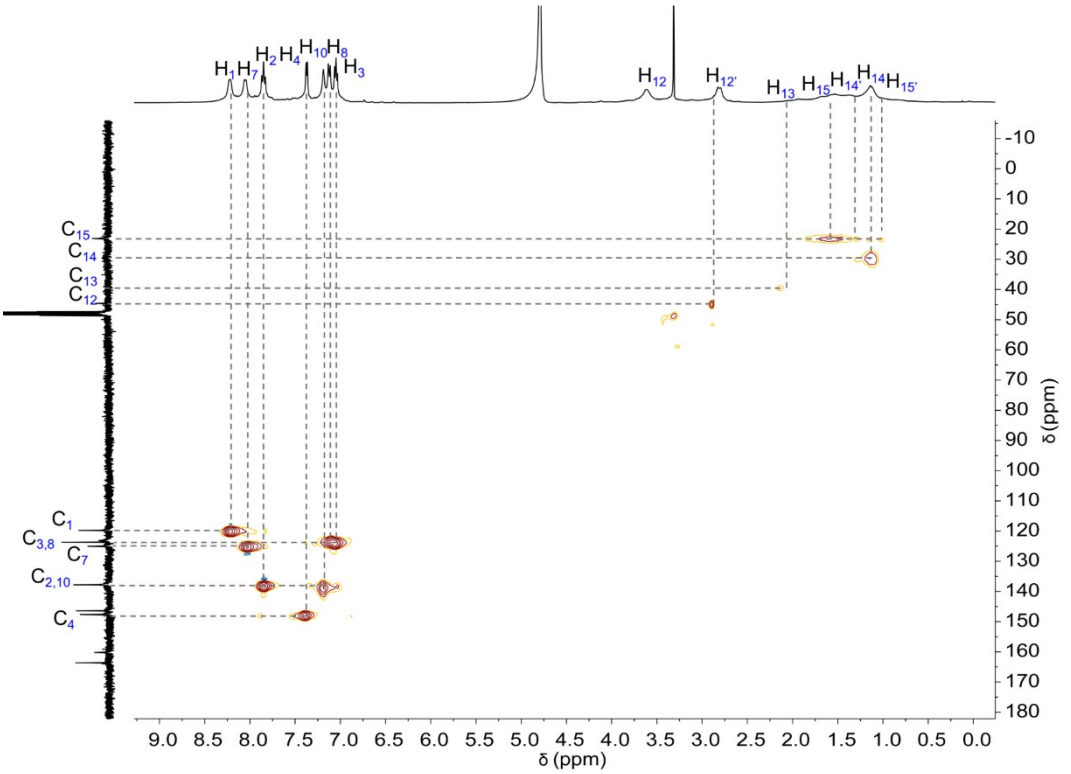

Fig. S28 ^{1}H-^{13}C HSQC spectrum (400 MHz, D_2O, 298K) of Δ_2R_6-**Hp**.

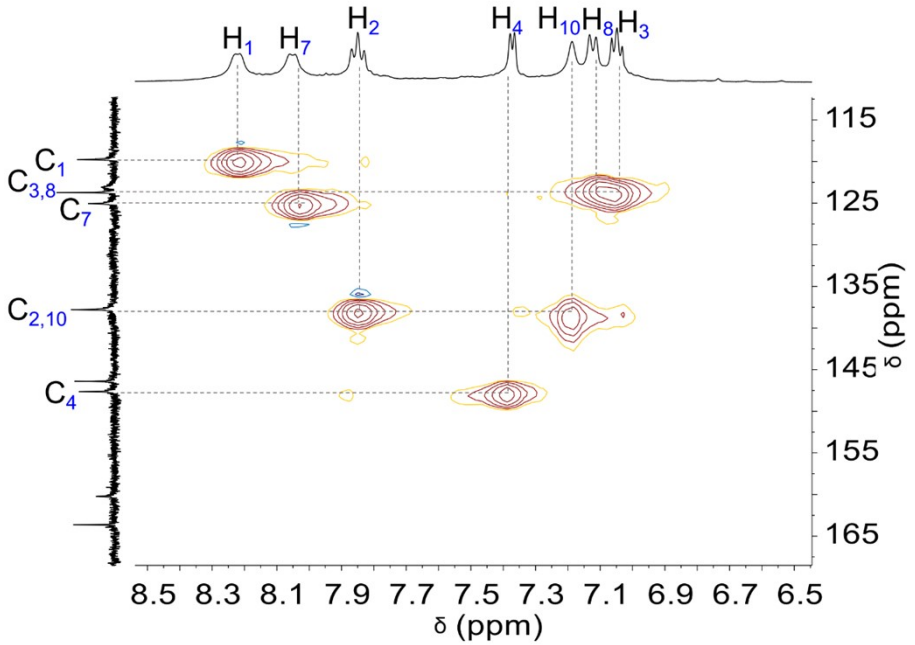

Fig. S29 Partial ^{1}H-^{13}C HSQC spectrum (400 MHz, D_2O, 298K) of Δ_2R_6-**Hp**.

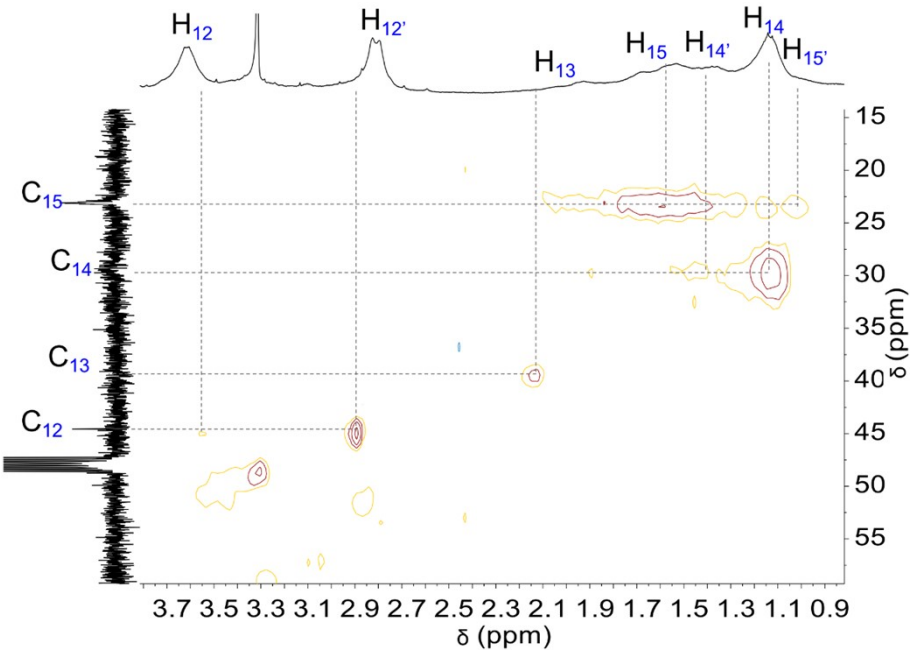

Fig. S30 Partial ^{1}H-^{13}C HSQC spectrum (400 MHz, D_2O, 298K) of Δ_2R_6-**Hp**.

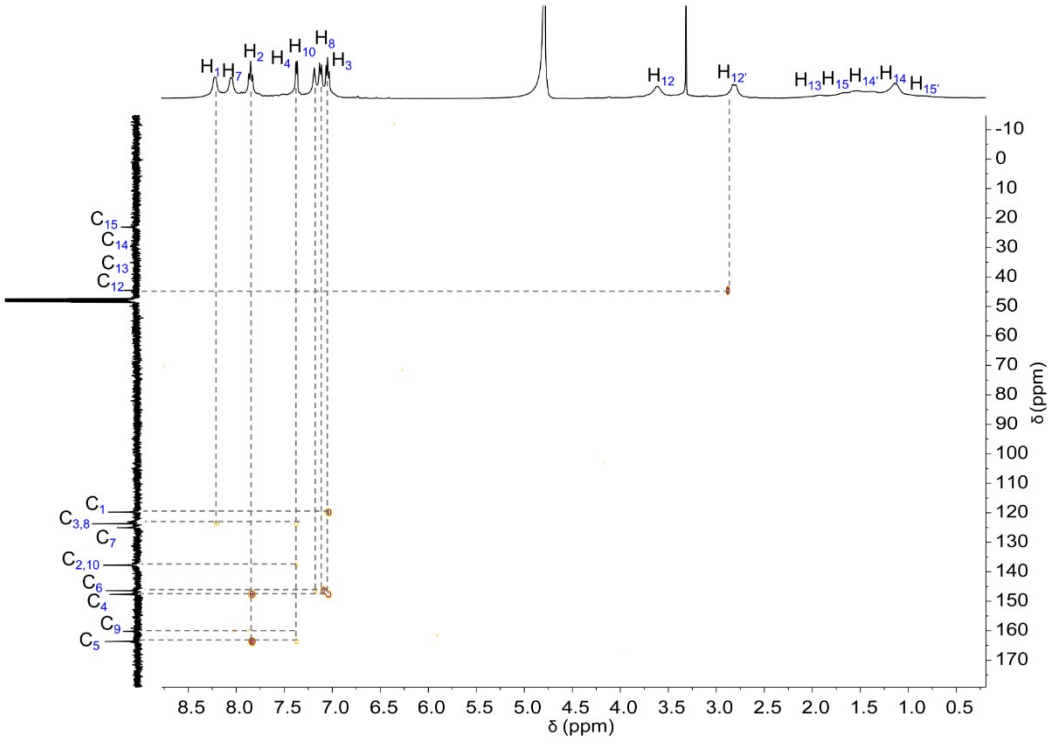

Fig. S31 ^{1}H-^{13}C HMBC spectrum (400 MHz, D_2O, 298K) of Δ_2R_6-**Hp**.

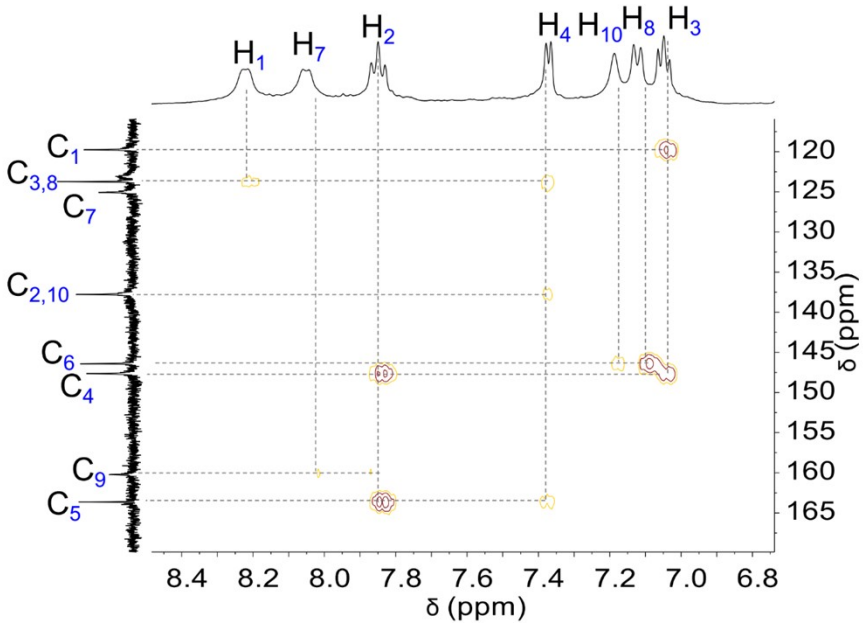

Fig. S32 Partial ^{1}H-^{13}C HMBC spectrum (400 MHz, D_2O, 298K) of Δ_2R_6-**Hp**.

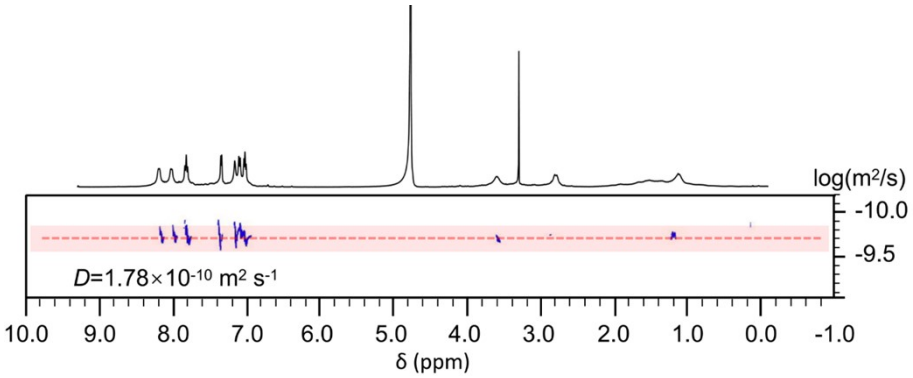

Fig. S33 ^{1}H DOSY NMR (400 MHz, D_2O, 298K) of Δ_2R_6-**Hp**.

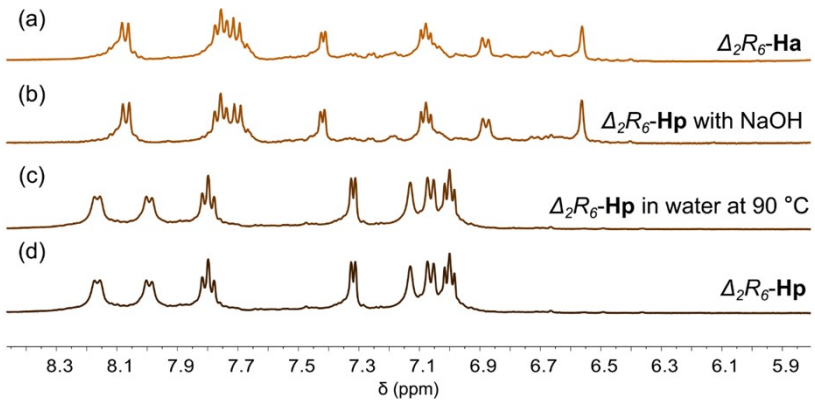

Fig. S34 (a) Partial ^{1}H NMR spectrum (400 MHz, DMSO-d_6) of Δ_2R_6-**Ha**. (b) Partial ^{1}H NMR spectrum (400 MHz, DMSO-d_6) of Δ_2R_6-**Hp** with NaOH. (c) Partial ^{1}H NMR spectrum (400 MHz, D_2O) of Δ_2R_6-**Hp** in 90 ℃ hot water for 48 h. (d) Partial ^{1}H NMR spectrum (400 MHz, D_2O) of Δ_2R_6-**Hp**.

4.2 Synthesis and characterization of Λ_2S_6-Hp

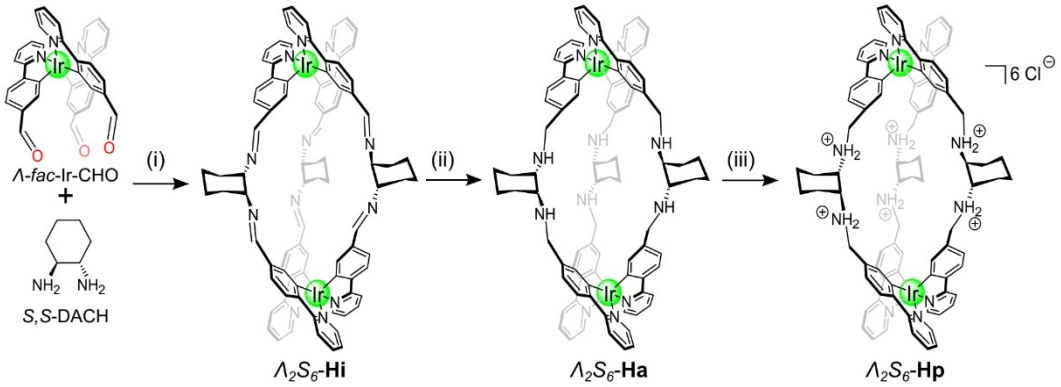

Scheme S5 Synthesis of enantiomeric Λ_2S_6-**Hp**. Reaction conditions: (i) p-Toluenesulfonic acid (TsOH), CH_3CN, Toluene, 110 °C, 12 h, 90% in total; (ii) $NaBH_4$, MeOH, CH_2Cl_2, rt, 12 h, 93%; (iii) HCl 0.1 M, MeOH, room temperature, 98%.

Λ_2S_6-**Hp** was successfully synthesized following the process of Λ_2R_6-**Hp**, through the substitution of the chiral modules with their corresponding enantiomers, in detail, Δ-*fac*-Ir-CHO was replaced by Λ-*fac*-Ir-CHO and *R,R*-DACH by *S,S*-DACH.

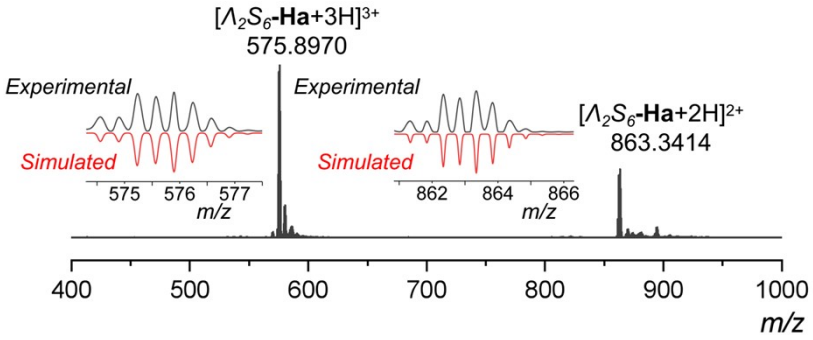

Fig. S35 HR-Q-TOF-MS spectrum of Λ_2S_6-**Ha**.

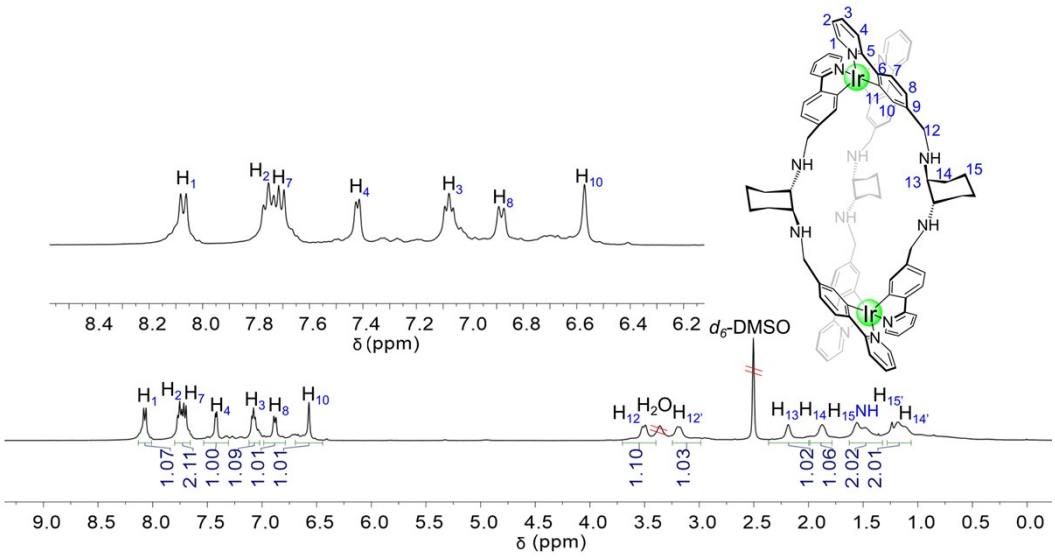

Fig. S36 ^{1}H NMR (400 MHz, DMSO-d_6, 298 K) spectrum of Λ_2S_6-**Ha**.

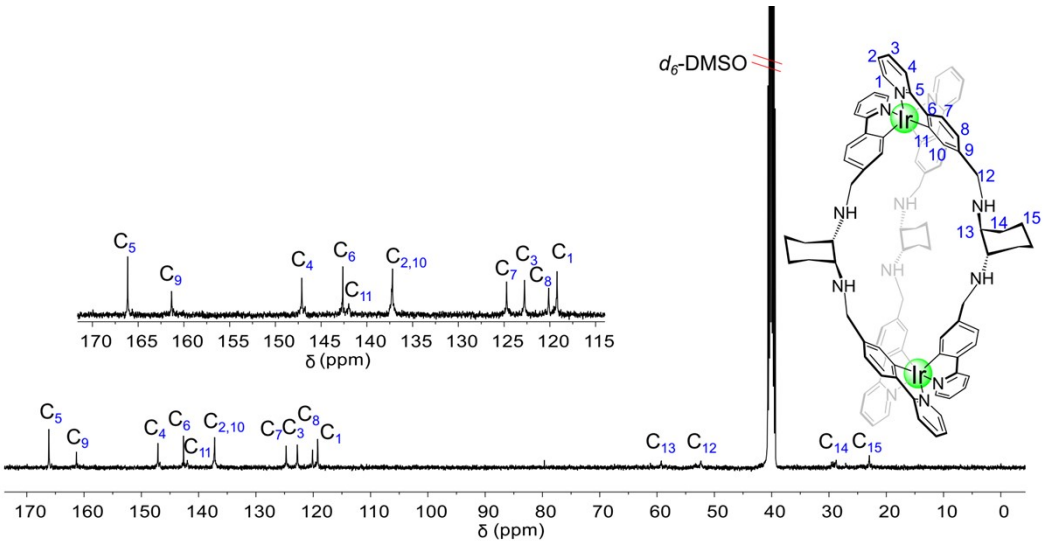

Fig. S37 ^{13}C NMR spectra (101 MHz, DMSO-d_6, 298K) of Λ_2S_6-**Ha**.

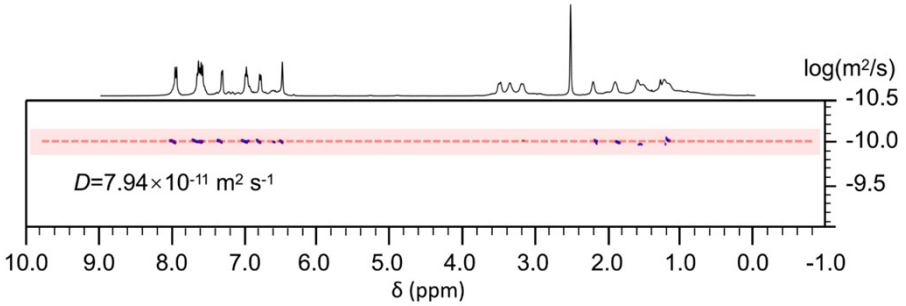

Fig. S38 ^{1}H DOSY NMR (400 MHz, DMSO-d_6, 295 K) spectrum of Λ_2S_6-**Ha**.

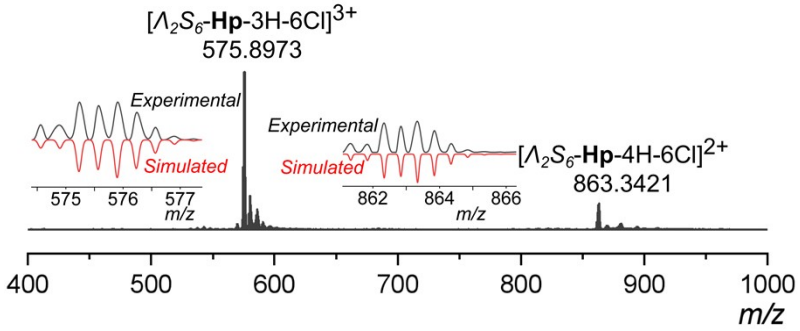

Fig. S39 HR-Q-TOF-MS spectrum of Λ_2S_6-**Hp**.

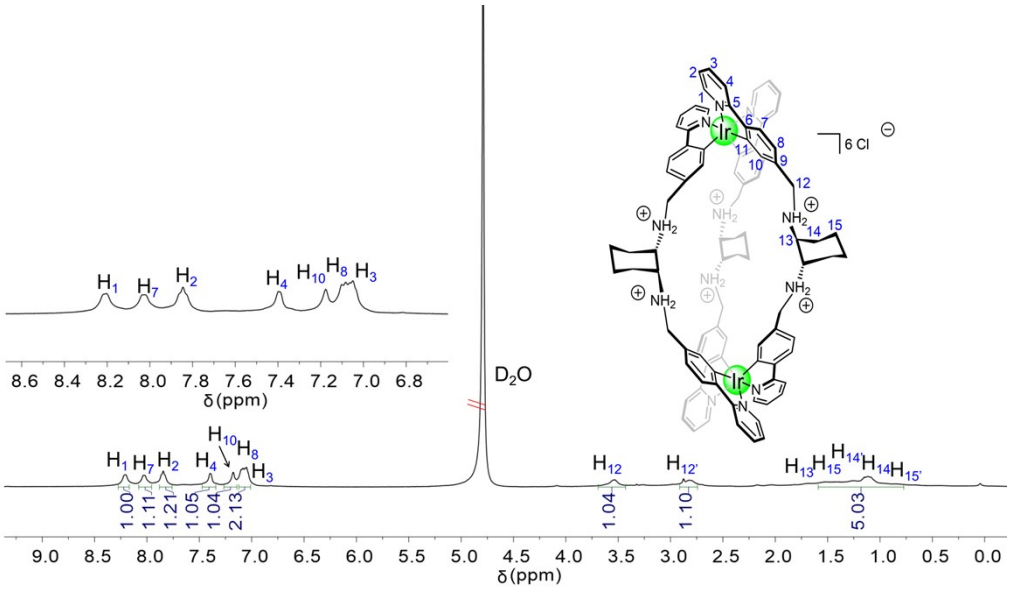

Fig. S40 ^{1}H NMR (400 MHz, D_2O, 298 K) spectrum of Λ_2S_6-**Hp**.

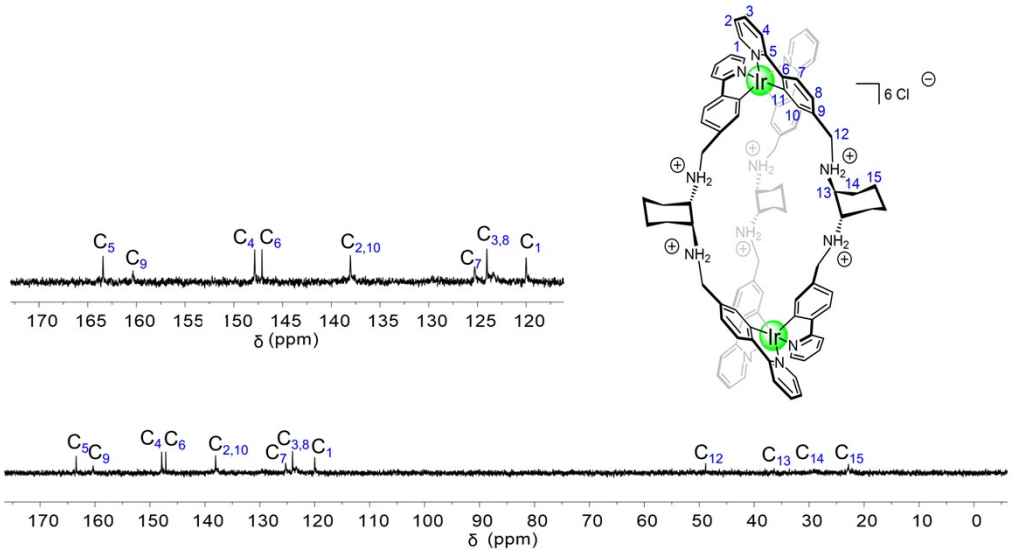

Fig. S41 ^{13}C NMR spectra (101 MHz, D_2O, 298K) of Λ_2S_6-**Hp**.

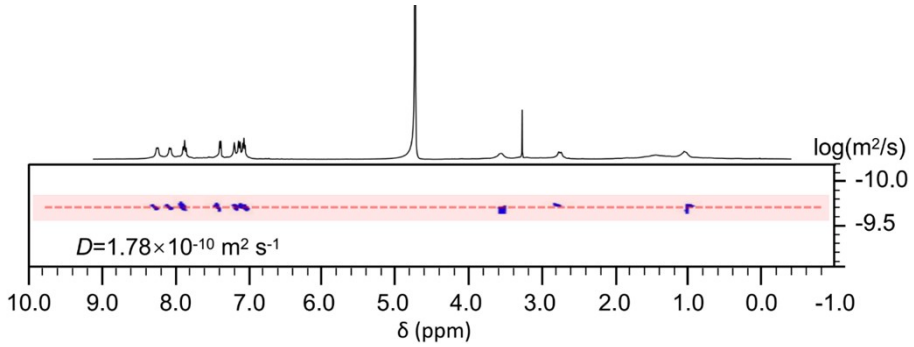

Fig. S42 ^{1}H DOSY NMR (400 MHz, D_2O, 298K) of Λ_2S_6-**Hp**.

4.3 CD and CPL characterization

Note: In DMSO solution, all enantiopure cages exhibited mirror-image circular dichroism (CD) and circularly polarized luminescence (CPL) spectra with robust Cotton effects, closely resembling those of the initial mononuclear *Δ*-/*Λ*-*fac*-Ir-CHO modules. [S12] The highly symmetrical and similar CD and CPL curves suggest that the pseudo-octahedral iridium stereochemistry of the starting *Δ*-/*Λ*-*fac*-Ir-CHO modules was well preserved during the assembly process, dominating the chirality of these enantiopure cages. These are confirmed that the chiral enantiomeric cages were successfully synthesized.

Quite interesting observations were made when characterizing the homochiral cages using CD and CPL spectroscopies. All homochiral cages resulted in chirality amplification, while the *Δ*-/*Λ*-*fac*-Ir-CHO modules presented weaker signals in comparison. As shown in Fig. S43a, Δ_2R_6-/Λ_2S_6-**Ha** presented more pronounced CD bands in the region of 300–340 nm, which was 2.6 times of the *Δ*-/*Λ*-*fac*-Ir-CHO modules. Such drastic enhancement might be attributed to the transfer of stereogenic information from the rigid C=N bonds of DACH ligands as well as the twisted structure. Moreover, the global transfer of chiral information throughout the whole skeleton, these cages presented prominent CPL with dissymmetric factor *g*lum of ±0.0016~0.0020 at 520~540 nm (Fig. S43b).

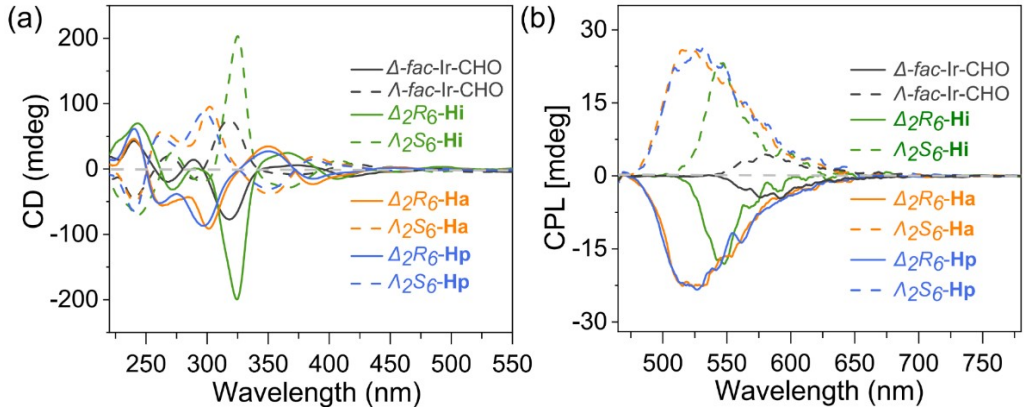

Fig. S43 CD and CPL spectra of chiral assembly modules and all enantiopure cages.

4.4 Synthesis and characterization of Au@Δ_2R_6-Hp

In detail, Δ_2R_6-**Hp** (12 mg, 0.006 mmol) was dissolved in deionized water (30 mL), followed by the addition of an aqueous $HAuCl_4$ solution (0.1 mL, 0.006 mmol) under an argon atmosphere with gentle stirring in the dark. The resulting mixture was stirred for 1 h to allow equilibration. During this period, the initially yellow solution exhibited minimal color change, suggesting that the $AuCl_4^-$ ions were likely encapsulated within the cavity of Δ_2R_6-**Hp**, driven by strong electrostatic interactions. Subsequent addition of NaOH (0.1 M, 0.6 mL) led to the formation of a yellow precipitate, corresponding to the neutral complex $AuCl_4^-$@Δ_2R_6-**Ha**. The solid was isolated by centrifugation and washed twice with water to remove unbound $AuCl_4^-$.

The resulting $AuCl_4^-$@Δ_2R_6-**Ha** powder was then treated with HCl (0.1 M, 0.6 mL) to protonate the host. Immediately thereafter, an aqueous $NaBH_4$ solution (5 mL, 0.012 mmol) was added

dropwise under vigorous stirring, affording a brown solution indicative of gold nanoparticle formation. This was followed by the addition of HCl (0.1 M) to adjust the pH to 2 under continued stirring. Finally, the mixture was freeze-dried to yield Au@***Δ*$_2$*R*$_6$*-Hp** as a dark yellowish-green powder. The gold content of was determined to be 25.9 wt% by inductively coupled plasma optical emission spectrometry (ICP-OES).

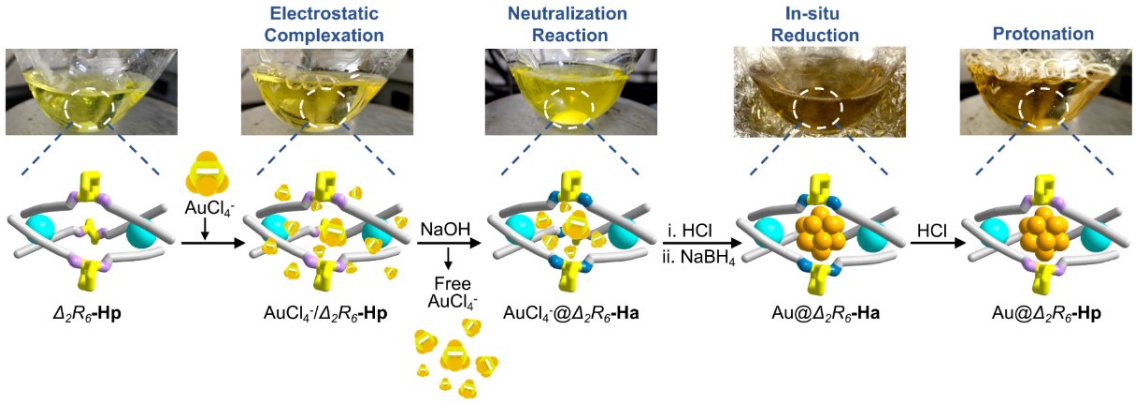

Scheme S6 the five-step strategy for synthesis of Au@*Δ*$_2$*R*$_6$**-Hp** involving Electrostatic complexation encapsulates $AuCl_4^-$ inclusion into the *Δ*$_2$*R*$_6$**-Hp** cavity, base treatment isolates the precipitate of Au@*Δ*$_2$*R*$_6$**-Ha** to remove un-encapsulated $AuCl_4^-$, and protonation the precipitate of $AuCl_4^-$@*Δ*$_2$*R*$_6$**-Ha** and re-dissolves in water, and in-situ $NaBH_4$ reduction with $AuCl_4^-$@*Δ*$_2$*R*$_6$**-Hp**, and followed by protonation of Au@*Δ*$_2$*R*$_6$**-Ha** to yield the final Au@*Δ*$_2$*R*$_6$**-Hp** product.

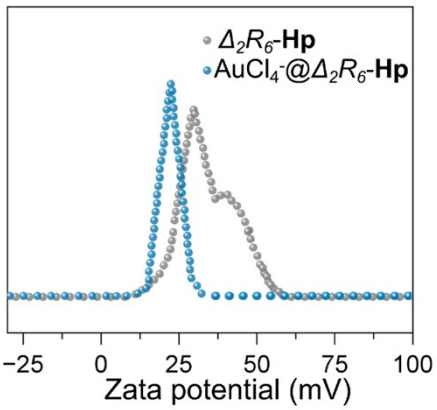

Fig. S44 Zeta potential curves of *Δ*$_2$*R*$_6$**-Hp** (gray) and $AuCl_4^-$@*Δ*$_2$*R*$_6$**-Hp** (blue).

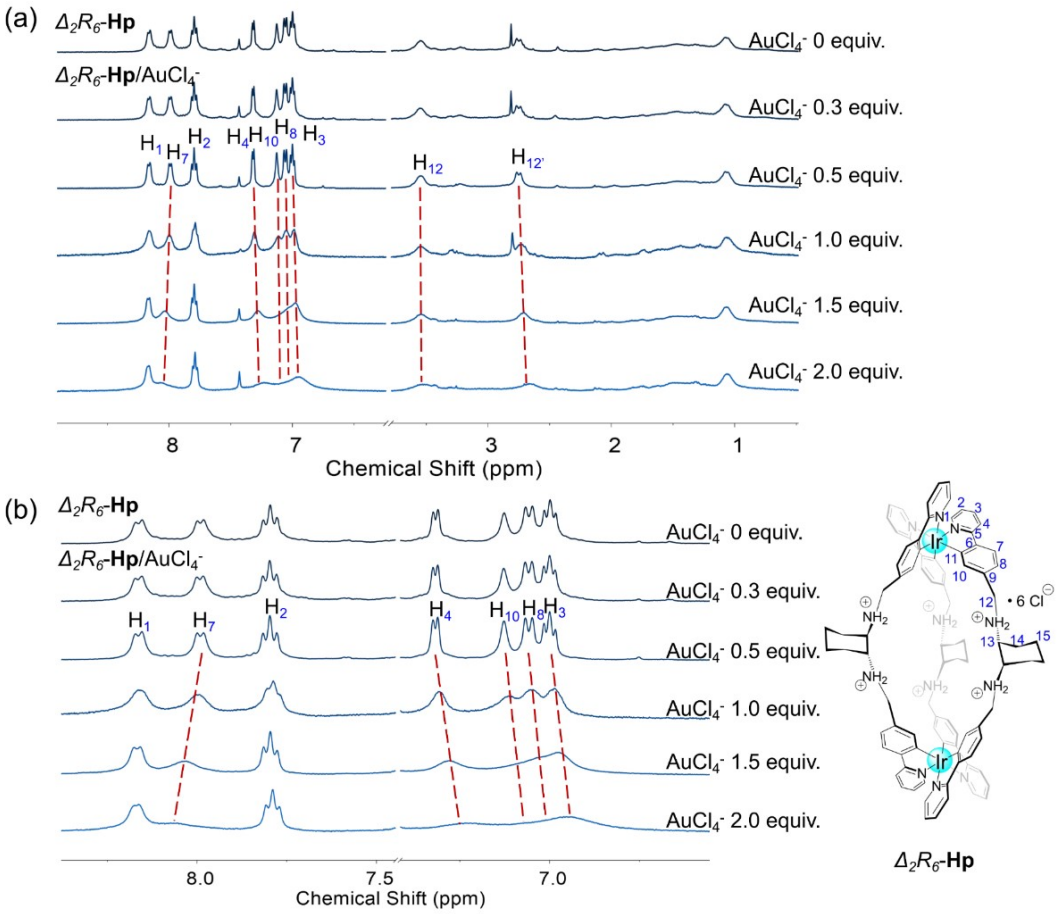

Fig. S45 (a) the ^{1}H NMR spectra to monitor the proton peaks shift to reveal the interaction between $AuCl_4^-$ anions and Δ_2R_6-**Hp**. (b) Enlarged areas for aromatic region peaks that clearly show the shifts migration.

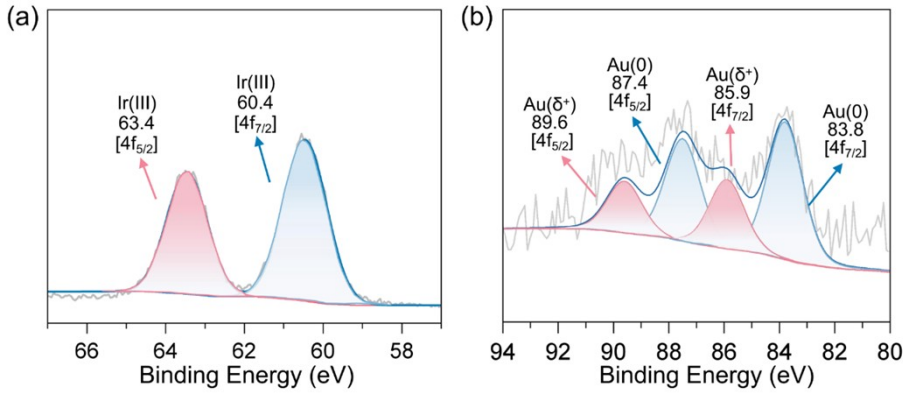

Fig. S46 (a) XPS spectrum of Ir 4f in Au@Δ_2R_6-**Hp**, showing the presence of Ir (III) at 60.4 eV for $4f_{7/2}$ and 63.4 eV for $4f_{5/2}$, respectively. (b) XPS spectrum of Au(0) 4f in Au@Δ_2R_6-**Hp**, showing the presence of Au(0) at 83.8 eV for $4f_{7/2}$ and 87.4 eV for $4f_{5/2}$, respectively; and the oxidative state of the Au(δ^+) 4f in Au@Δ_2R_6-**Hp**, showing the presence of Au(δ^+) at 85.9 eV for $4f_{7/2}$ and 89.6 eV for $4f_{5/2}$, respectively.

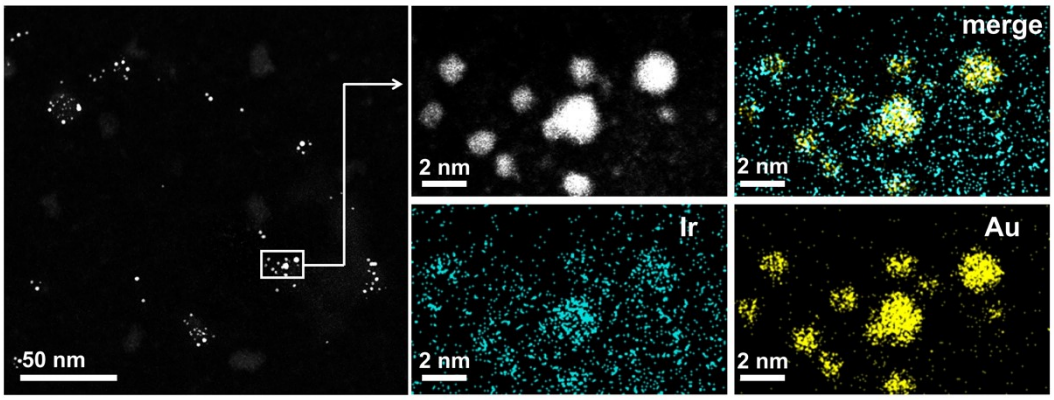

Fig. S47 HAADF-STEM image and corresponding EDS elemental mapping of Ir and Au for the Au@Δ_2R_6-**Hp**.

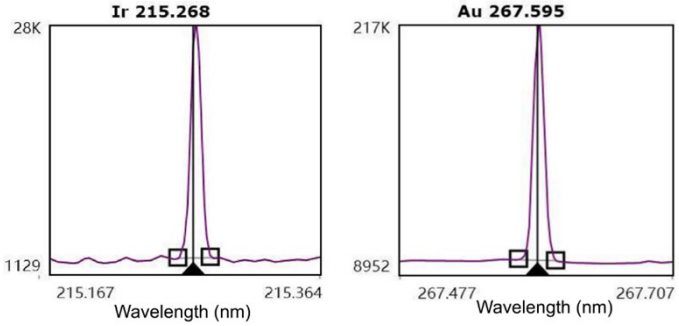

Analyte	Concentration	Units	Intensity
Ir 215.268	6.970	mg/L	72,952.6
Au 267.595	2.599	mg/L	557,257.8

Fig. S48 Inductively coupled plasma optical emission spectrometry (ICP-OES) of Au@Δ_2R_6-**Hp**. A gold loading of 25.9 wt% suggests incomplete occupancy of the protonated cages.

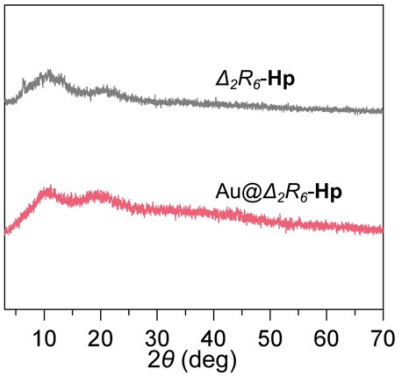

Fig. S49 PXRD patterns of Δ_2R_6-**Hp** (gray) and Au@Δ_2R_6-**Hp** (pink).

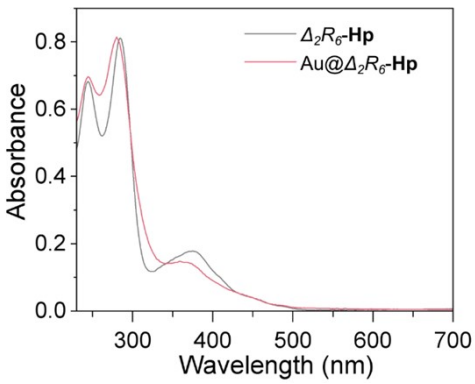

Fig. S50 UV-vis spectra of complexes Δ_2R_6-**Hp** and Au@Δ_2R_6-**Hp** in DMSO (10 μM).

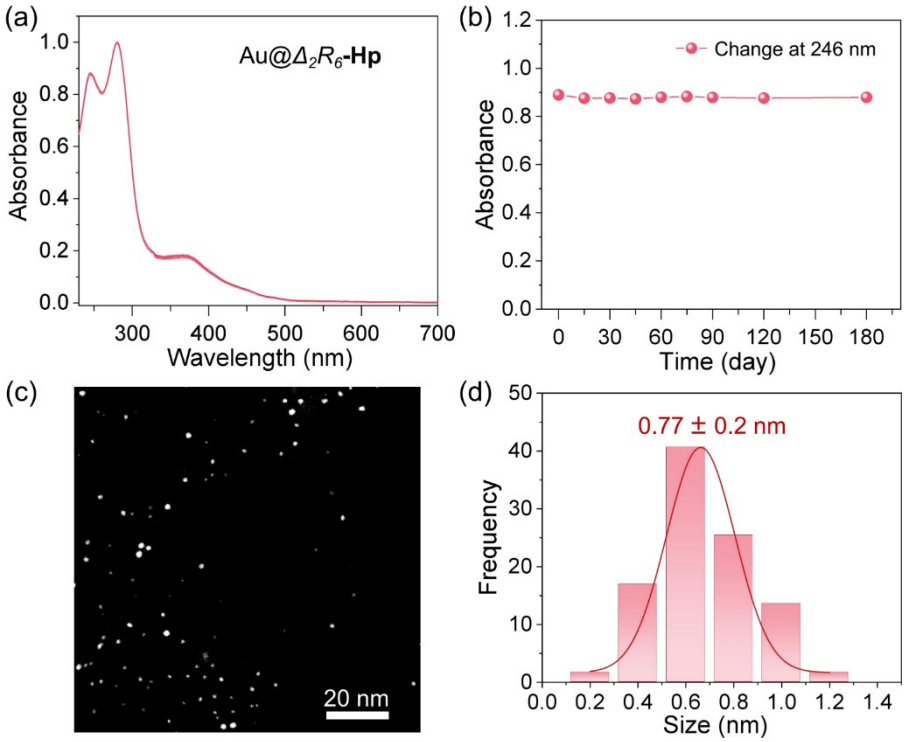

Fig. S51 (a) Evolution of the UV-vis spectra of Au@Δ_2R_6-**Hp** stored in the refrigerator at -4 ℃ in water for 180 days; (b) Time-dependent corresponding absorption of Au@Δ_2R_6-**Hp** at 246 nm. (c) HAADF-STEM image of Au@Δ_2R_6-**Hp** after 180 days. (d) HAADF-STEM images at scale bar of 20 nm corresponding statistical size distribution histogram of encapsulated Au clusters in Δ_2R_6-**Hp** after 180 days.

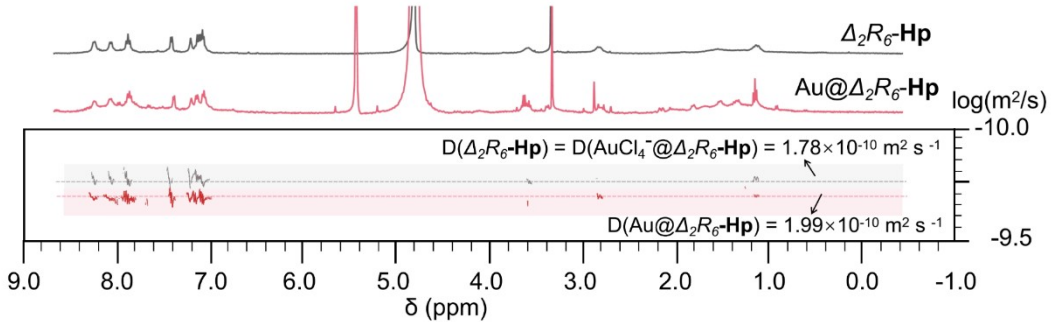

Fig. S52 ^{1}H NMR and DOSY spectra of Δ_2R_6-**Hp** (gray), $AuCl_4^-$@Δ_2R_6-**Hp** (blue) and Au@Δ_2R_6-**Hp** (pink).

4.5 Synthesis and characterization of Au@Λ_2S_6-Hp

The Λ_2S_6-**Hp** is also an ideal scaffold for the encapsulation and stabilization of Au-NCs. We successfully obtained Au@Λ_2S_6-**Hp** though the same process as Au@Δ_2R_6-**Hp**. The Au-NCs in Λ_2S_6-**Hp** are uniformly distributed and have homogeneous sizes, estimated to be 0.73 ± 0.18 nm.

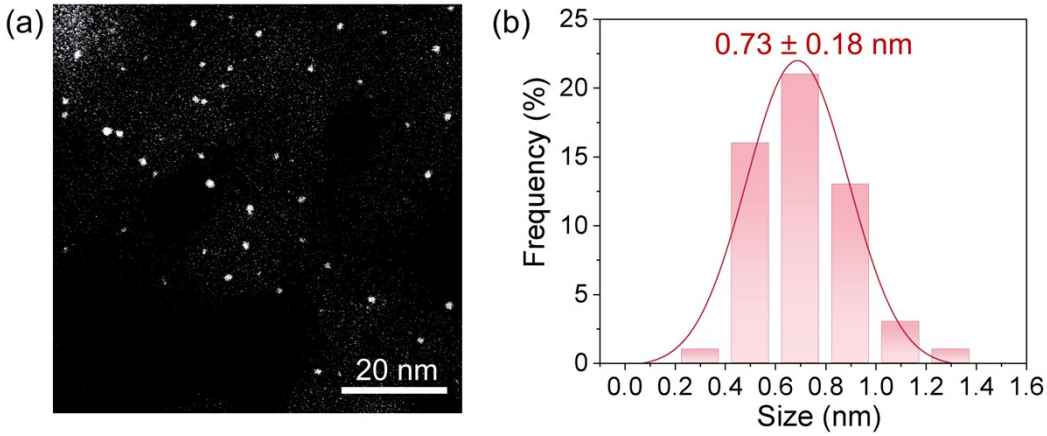

Fig. S53 (a, b) Spherical aberration HAADF-STEM images of Au@Λ_2S_6-**Hp**. (c) the corresponding size distribution histogram of Au clusters in Λ_2S_6-**Hp**.

4.6 Synthesis and characterization of Au/Δ_2R_6-Ha

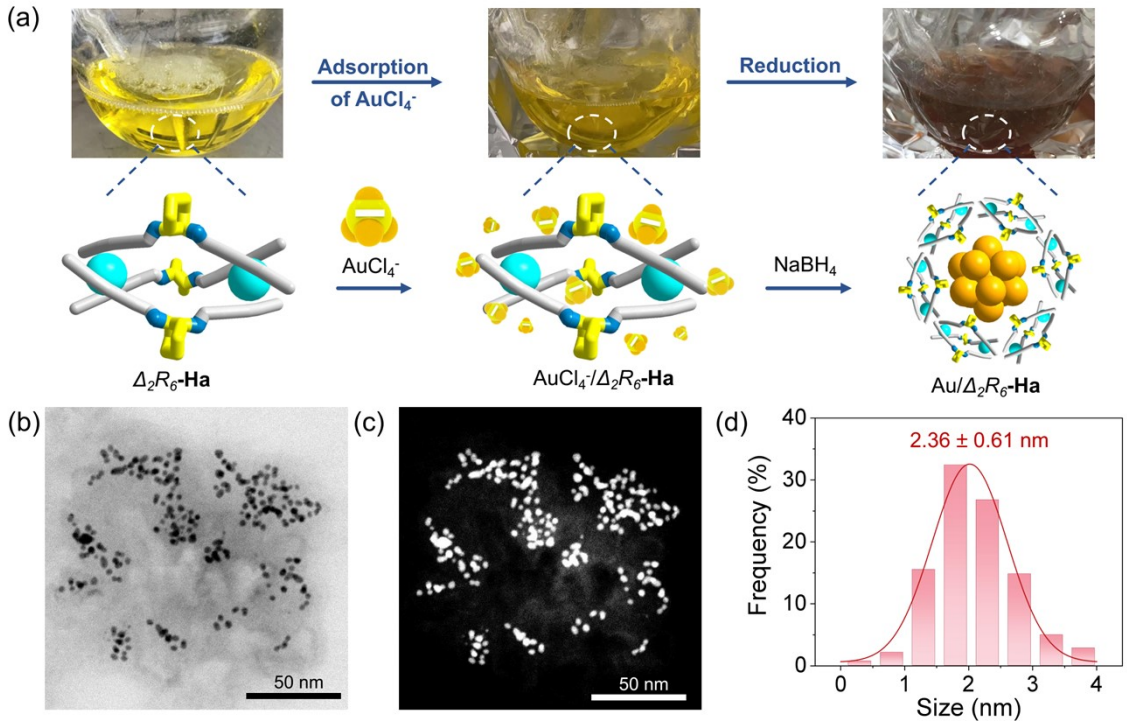

Fig. S54 (a) the synthesis of Au/Δ_2R_6-**Ha** involving (1) Adsorption of $AuCl_4^-$ onto the Δ_2R_6-**Ha**, (2) In-situ $NaBH_4$ reduction with $AuCl_4^-/\Delta_2R_6$-**Ha**. (b) STEM images and (c) HAADF-STEM images of Au/Δ_2R_6-**Ha**. (d) The corresponding size distribution histogram of Au nanoparticles immobilized on Δ_2R_6-**Ha**, scale bar: 50 nm.

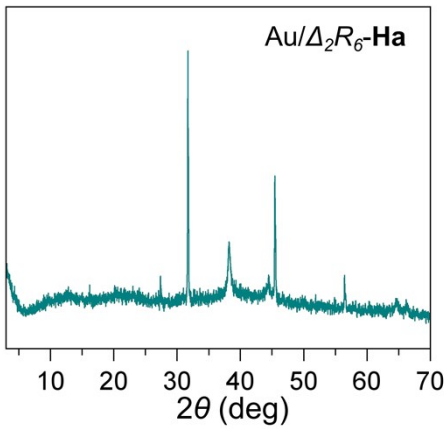

Fig. S55 PXRD patterns of Au/Δ_2R_6-**Ha**.

The synthesis of gold nanoparticles (2.36 ± 0.61 nm) using the reduced cage compound Δ_2R_6-**Ha** as a template carrier through the similar methodology (Fig. S54). Δ_2R_6-**Ha** (12 mg, 0.006 mmol) was dissolved in methanol (5 mL), dispersed in water (30 mL), subsequently added to 0.1 mL (0.006 mmol) of aqueous $HAuCl_4$ solution (21.5 mg in 1 mL water), dark stirring in Ar atmosphere. The yellow solution gradually deepened in color, and then 5 mL of aqueous solution containing $NaBH_4$

(4.6 mg, 0.012 mmol, 20 equiv.) was immediately added dropwise with vigorous shaking, resulting in a brown solution. Afterward, the methanol was evaporated at room temperature, and the product was freeze-dried to yield Au/Δ_2R_6-**Ha** as a dark brown powder. The PXRD pattern of Au/Δ_2R_6-**Ha** shows multiple diffraction peaks in the 30-70° range, consistent with the presence of crystalline Au nanoparticles (Fig. S55). The size difference occurs because Δ_2R_6-**Ha** loses the capacity to trap metal anion precursors through strong electrostatic attraction, unlike its protonated counterpart. These complementary datasets provide robust evidence for the maintained nanoparticle retention and dispersion stability.

Section 5. Evaluation of Catalytic Performance

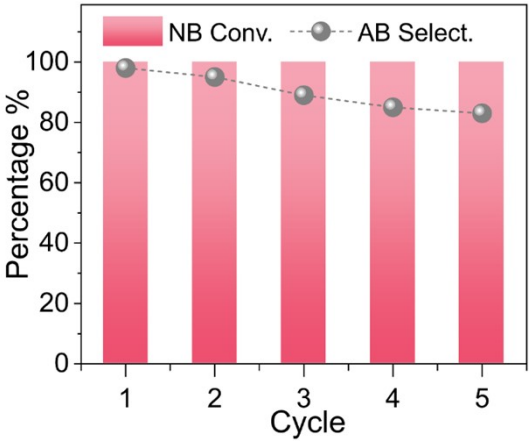

Fig. S56 Recycle experiments of Au@Δ_2R_6-**Hp**, each cycle was conducted for 24 h.

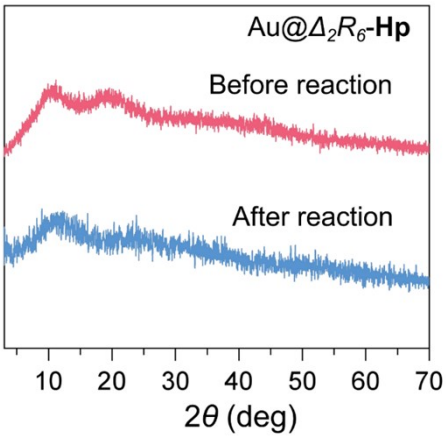

Fig. S57 PXRD pattern of the freshly prepared Au@Δ_2R_6-**Hp** (pink line) and after catalytic cycles (blue line), the two broad bands in the range of 10-30° were retained after reaction, also suggesting that the skeleton of Δ_2R_6-**Hp** is maintained. The identical PXRD patterns no diffraction peaks of Au crystallite peaks are observed after the reaction, confirming the remarkable stability of the nanoclusters against aggregation.

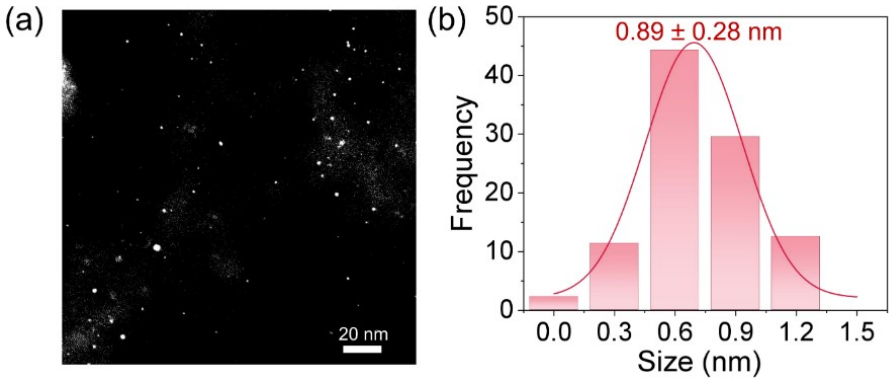

Fig. S58 HAADF-STEM images of Au@Δ_2R_6-**Hp** after catalytic cycles and the corresponding size distribution histogram of Au-NCs, revealing a size of 0.89 ± 0.28 nm.

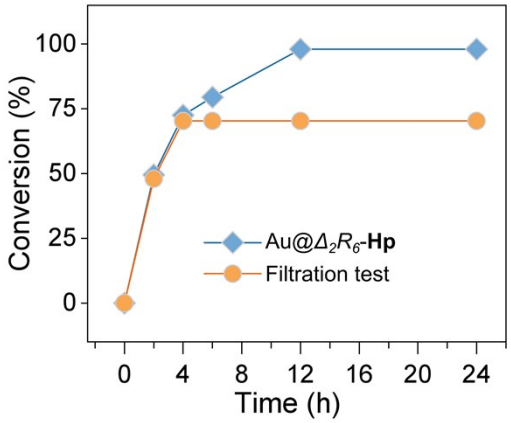

Fig. S59 Time-dependent conversion of **AOB** and **AB** during **NB** reduction under standard conditions using Au@Δ_2R_6-**Hp** (blue line), and after its removal by filtration at 4 h (orange line).

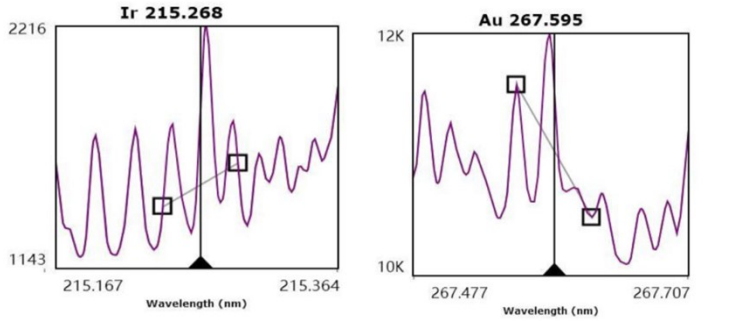

Analyte	Concentration	Units	Intensity
Ir 215.268	0.1056	mg/L	1,224.0
Au 267.595	0.0122	mg/L	2,200.2

Fig. S60 ICP-OES analysis of the supernatant after the **NB** reduction reaction following removal of Au@Δ_2R_6-**Hp**, indicating negligible loss of Au during catalysis.

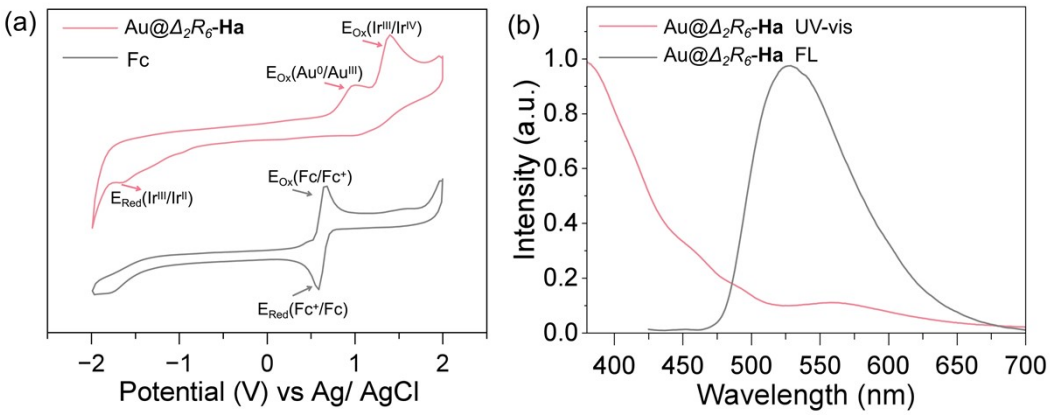

Fig. S61 (a) Cyclic voltammograms of Au@Δ_2R_6-**Hp** and **Fc** in dry CH_3CN solution containing 0.1 M *n*-Bu_4NPF_6 under N_2 atmosphere, showing redox couples of +1.18 and -1.80 (V *vs* Ag/AgCl) for Ir^{IV}/Ir^{III}. (b) Normalized absorption and emission spectra of Au@Δ_2R_6-**Hp** ($E_{0\text{-}0}$ = 2.55 eV).

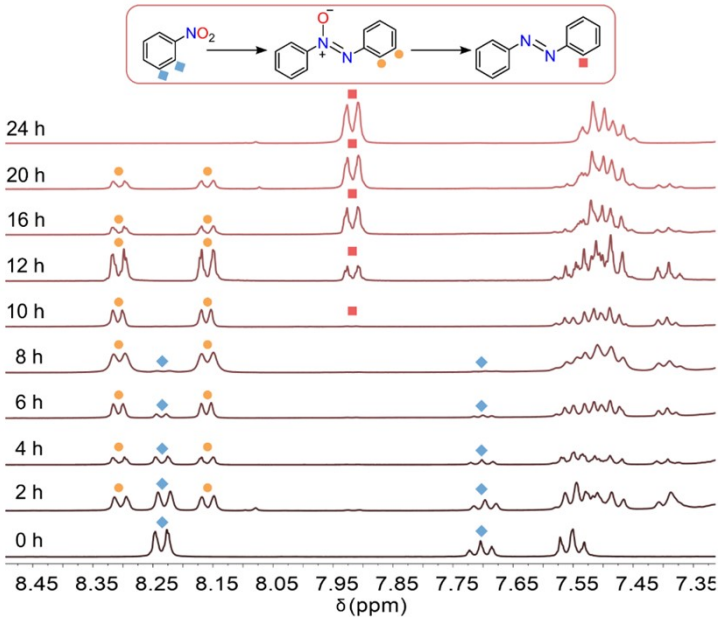

Fig. S62 ^{1}H NMR analysis of the catalytic transfer of **NB** to **AB** by Au@Δ_2R_6-**Hp** at different times (0-24 h) recorded in $CDCl_3$.

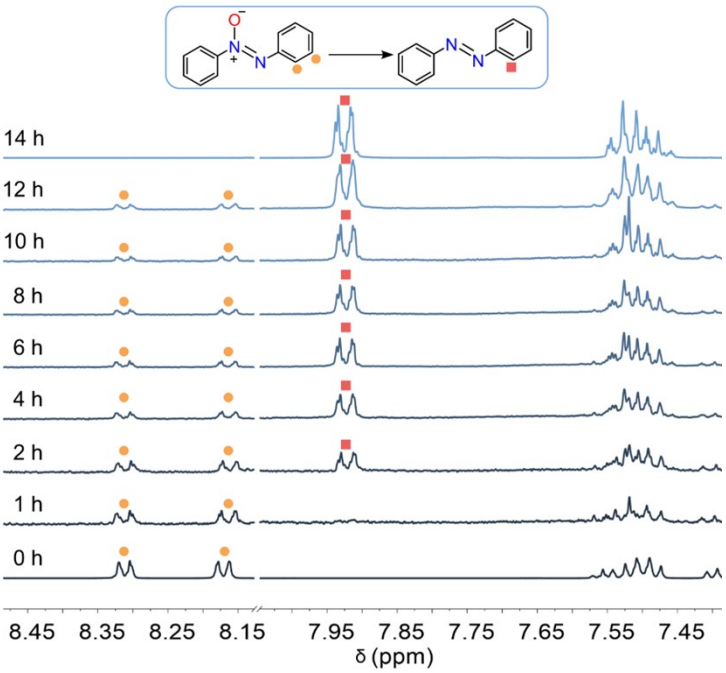

Fig. S63 ^{1}H NMR analysis of the catalytic transfer of **AOB** to **AB** by Au@Δ_2R_6-**Hp** at different times (0-14 h) recorded in $CDCl_3$.

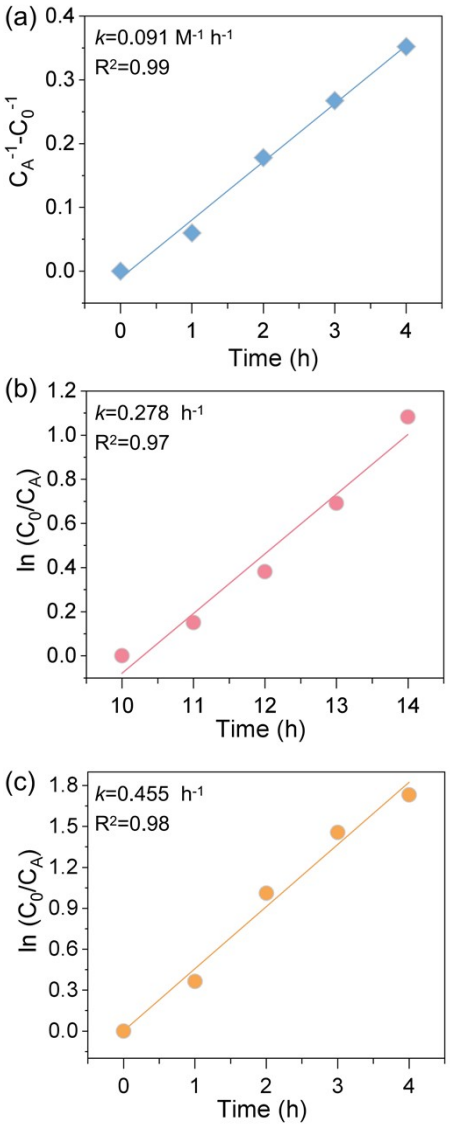

Fig. S64 Kinetic analysis of Au@Δ_2R_6-**Hp** catalyzed reactions: (a) **NB** reduction (0-4 h); (b) **NB** reduction (10-14 h); and (c) **AOB** reduction (0-4 h).

Note: To experimentally probe **NB** involvement, kinetic studies were carried out by varying the initial NB concentration (0.05-0.15 mmol) while keeping other conditions constant. Conversion was measured at 30 min and remained below 20%. The apparent initial rate (v_0) was calculated according to:

$$v_0 = \frac{C_0 - C_t}{t}$$

where C_0 and C_t denote the initial and remaining **NB** concentrations, respectively, and t = 0.5 h.

As shown in Fig. S62, a log-log plot of v_0 versus C_0 displays a linear relationship. Linear regression yields a slope of 2.247 with $R^2 = 0.98$, indicating an apparent second-order dependence on **NB** concentration. This kinetic behavior supports the formation of a reaction intermediate involving two **NB** molecules.

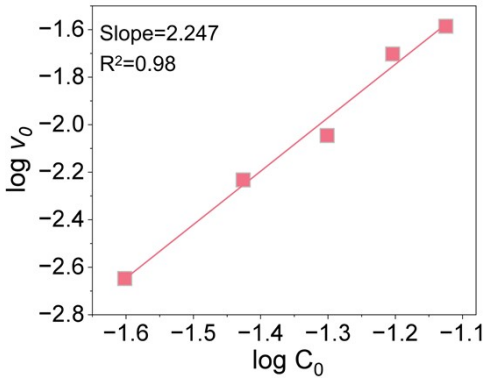

Fig. S65 Log-log plot of the apparent initial rate (v_0) versus the initial **NB** concentration (C_0).

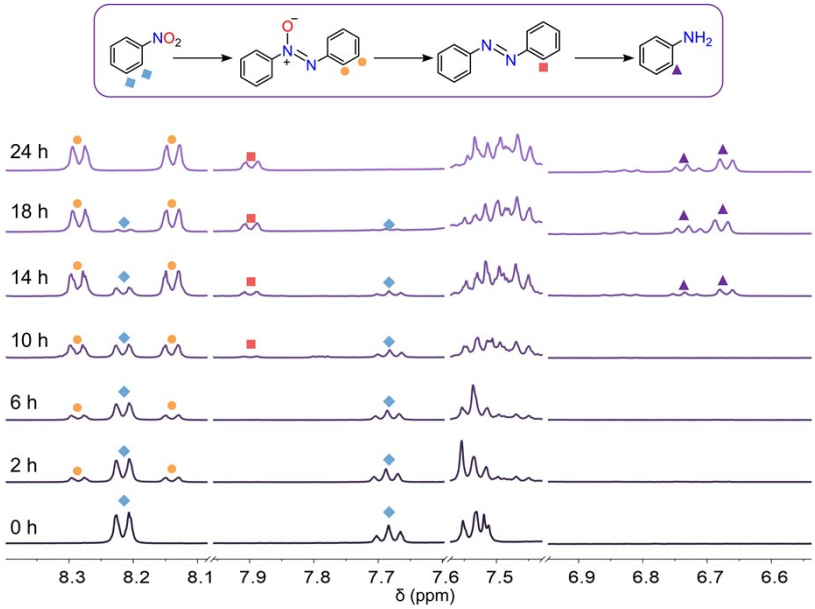

Fig. S66 ^{1}H NMR analysis of the catalytic transfer of **NB** to **AB** by Au/Δ_2R_6-**Ha** at different times (0-24 h) recorded in $CDCl_3$.

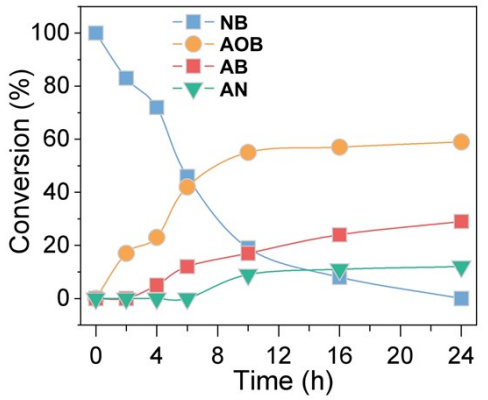

Fig. S67 Kinetic variation of the **NB** reduction catalyzed by Au/Δ_2R_6-**Ha**.

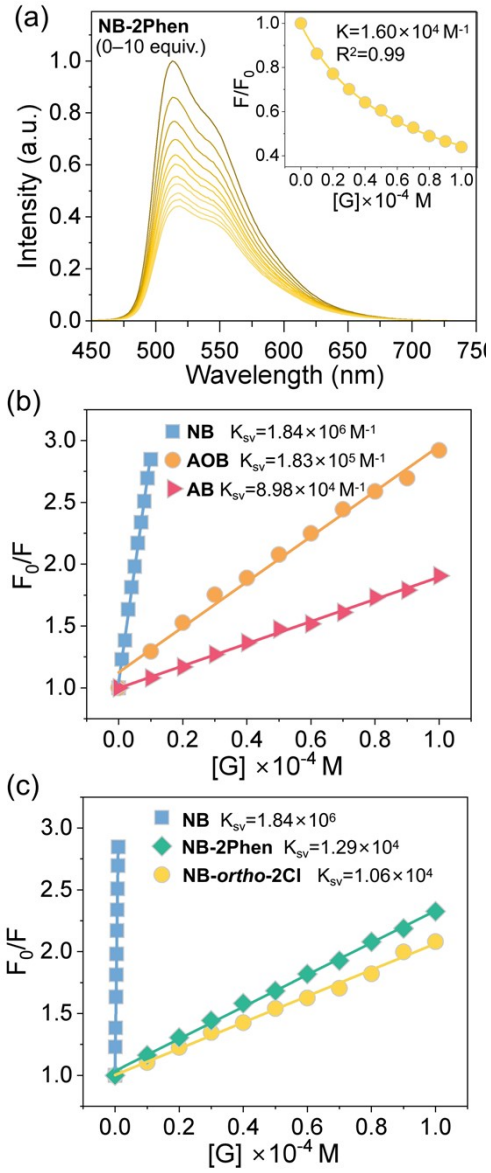

Fig. S68 (a) Fluorescence quenching spectra of Au@Δ_2R_6-**Ha** (1.0×10^{-5} M) titrated with **NB-2Phen** (0–10 equiv.). (b) Stern-Volmer plots for fluorescence quenching of Au@Δ_2R_6-**Ha** by **NB**, **AOB** and **AB**. (c) Stern-Volmer plots for fluorescence quenching of Au@Δ_2R_6-**Ha** by **NB**, **NB-*ortho*-2Cl** and **NB-2Phen**. F_0 and F are the emission intensity in the absence and presence of substrate, respectively; [G] is the concentration of the substrate. Binding (K) and Stern-Volmer constants (K_{SV}) have been calculated using previously reported equations. [S1, S2]

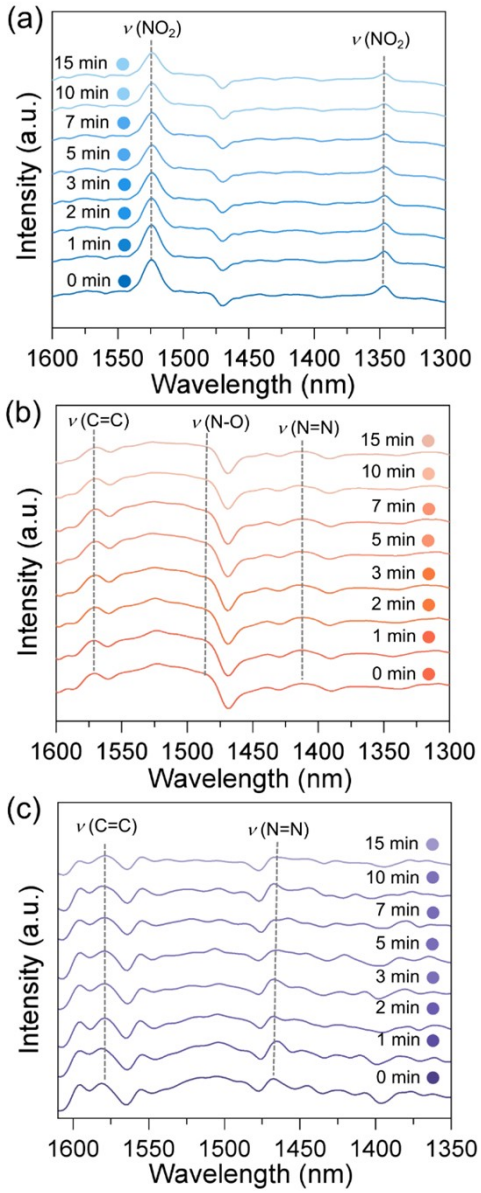

Fig. S69 Time-dependent DRIFTS desorption of (a) **NB**, (b) **AOB** and (c) **AB** on Au@Δ_2R_6-**Ha**.

Section 6. Computational Studies

6.1 Geometric structures optimized

6.11 Geometry-optimized structure of Δ_2R_6-Ha and Δ_2R_6-Hp

Note: The observed differences in cavity dimensions of Δ_2R_6-**Hp** arise from the electrostatic interactions, which modulate the cage geometry.

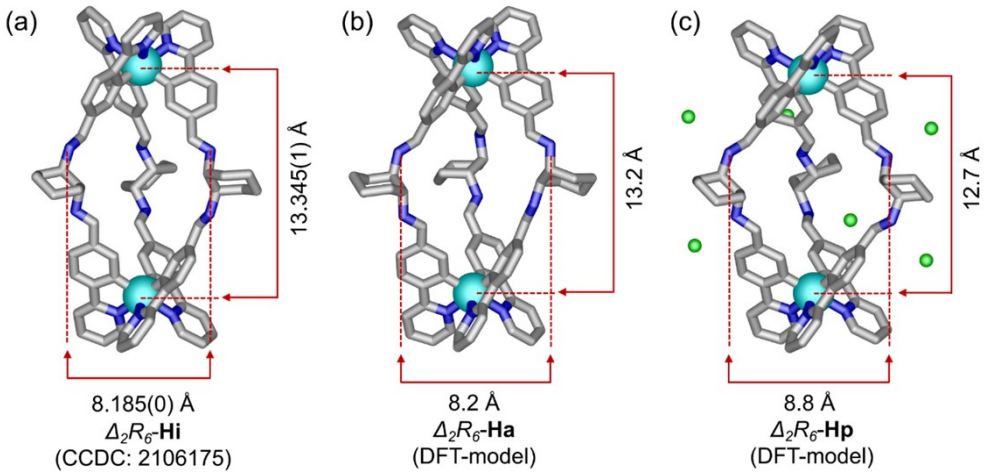

Fig. S70 Geometry-optimized structure of Δ_2R_6-**Ha** and Δ_2R_6-**Hp**. Color code: Ir atom: cyan; N atom: blue; C atom: grey; Cl atom: green.

6.12 Geometry-optimized structure of Au@Δ_2R_6-Ha

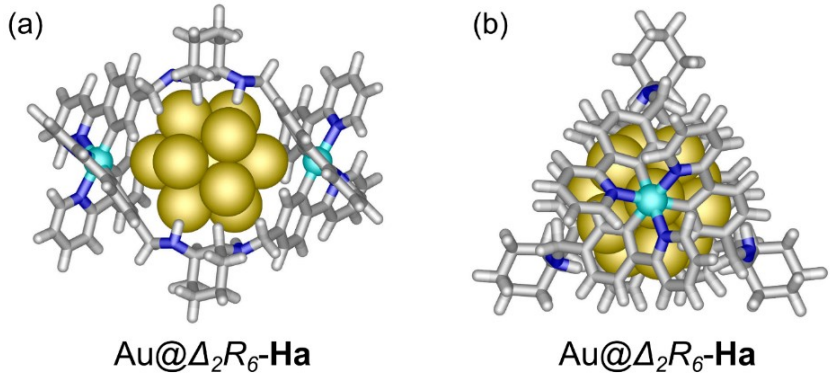

Fig. S71 Geometry-optimized structure of Au@Δ_2R_6-**Ha**. Color code: Ir atom: cyan; Au-NCs: yellow; N atom: blue; C atom: grey; H atom: light grey.

6.13 Adsorption geometries

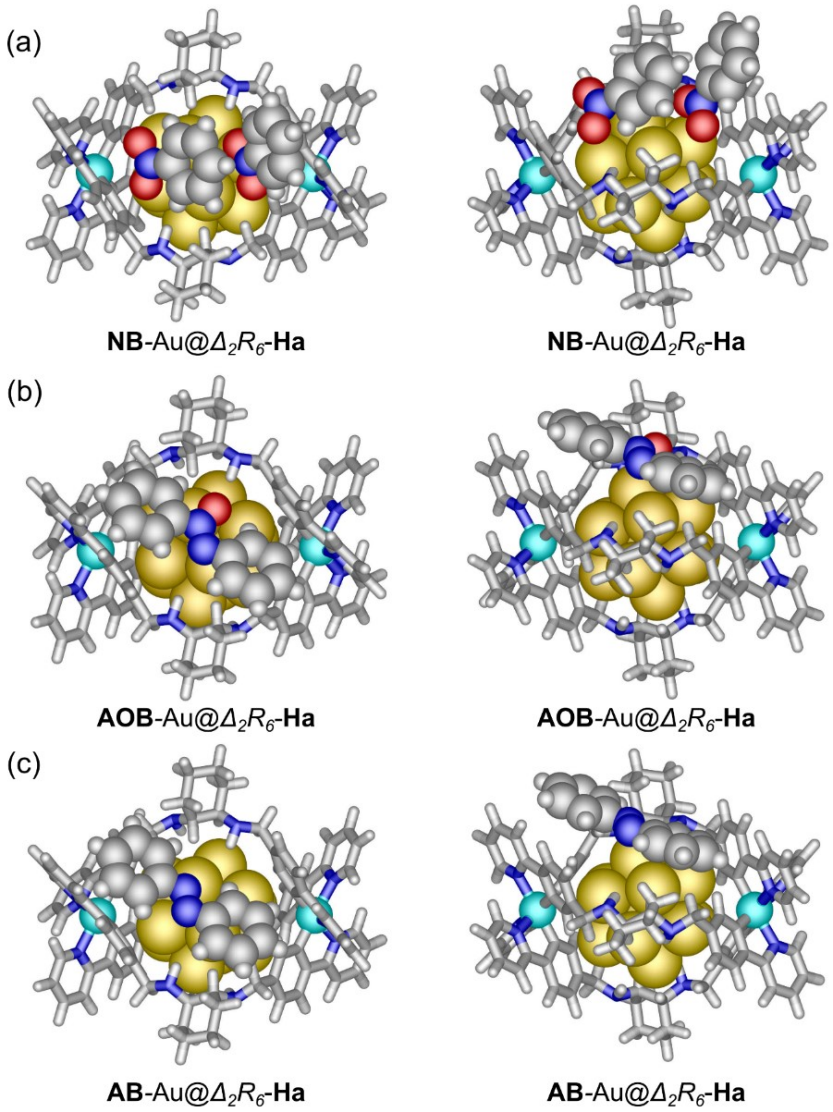

Fig. S72 Adsorption geometries of (a)**NB**, (b) **AOB** and (c) **AB** on Au-NCs surface of Au@Δ_2R_6-**Ha**. Color code: Ir atom: cyan; Au-NCs: yellow; N atom: blue; O atom: red; C atom: grey; H atom: light grey.

6.2 Reaction energies calculations

Note: The reaction pathways from nitrobenzene to azobenzene on the Au@Δ_2R_6-**Ha** and the corresponding energy profiles were calculated. With Au@Δ_2R_6-**Ha**, the adsorbed two **NB** can be to form ***NB**s with reaction energy of -2.35 eV. Subsequent transfer of six H* to two ***NB**s can give rise to adsorbed ***AOB**, which feature reaction energies of -2.58 eV. Subsequently, the ***AOB** intermediate would be reduced to ***AB** with an energy barrier of -1.40 eV. To evaluate the feasibility of further conversion, the hydrogenation of ***AB** to *2**AN** was calculated, revealing a high energy barrier of 3.62 eV. This significant barrier, combined with the elevated desorption energy of **AN** (2.44 eV), confirms the thermodynamic difficulty of 2**AN** formation in this system. The desorption energy of ***AB** from Au-NCs (1.92 eV) is significantly lower than the activation barrier for its

hydrogenation to *2**AN** (3.62 eV). These computational results perfectly align with experimental observations, revealing that Au@Δ_2R_6-**Ha** selectively catalyzes **NB**-to-**AB** conversion through this energetically favorable pathway while intentionally preventing over-reduction.

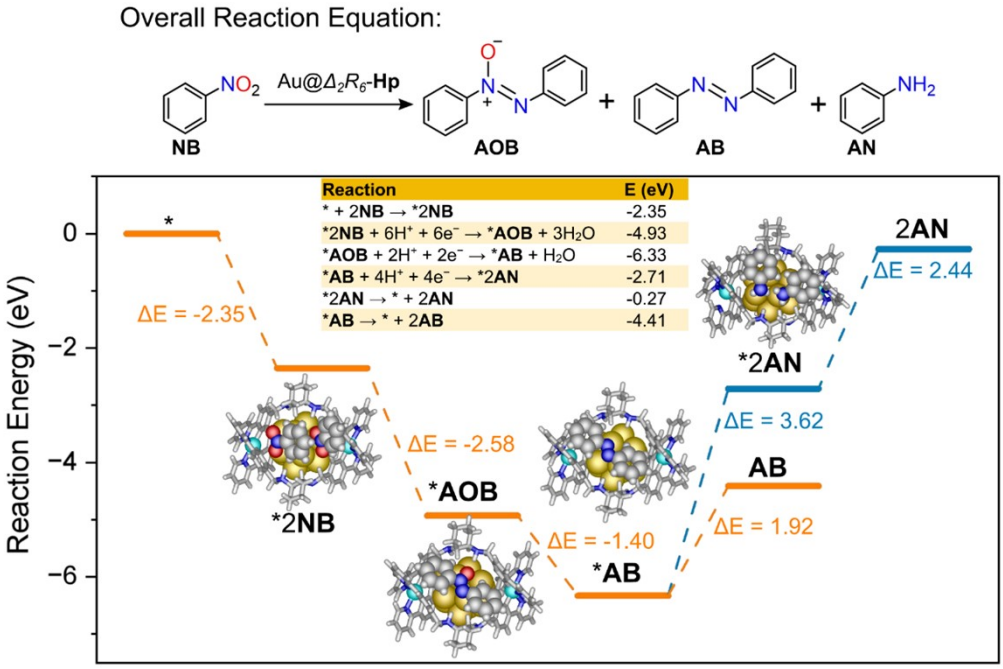

Fig. S73 Relative energy variation along the reaction pathway for Au@Δ_2R_6-**Ha**. The inserted table is the reaction energy corresponding to specific reaction steps and figures are the optimized models of substrate/ product adsorption on the catalyst. Color code: Ir atom: cyan; Au-NCs: yellow; N atom: blue; O atom: red; C atom: grey; H atom: light grey.

Section 7. ^{1}H NMR spectra of catalytic products

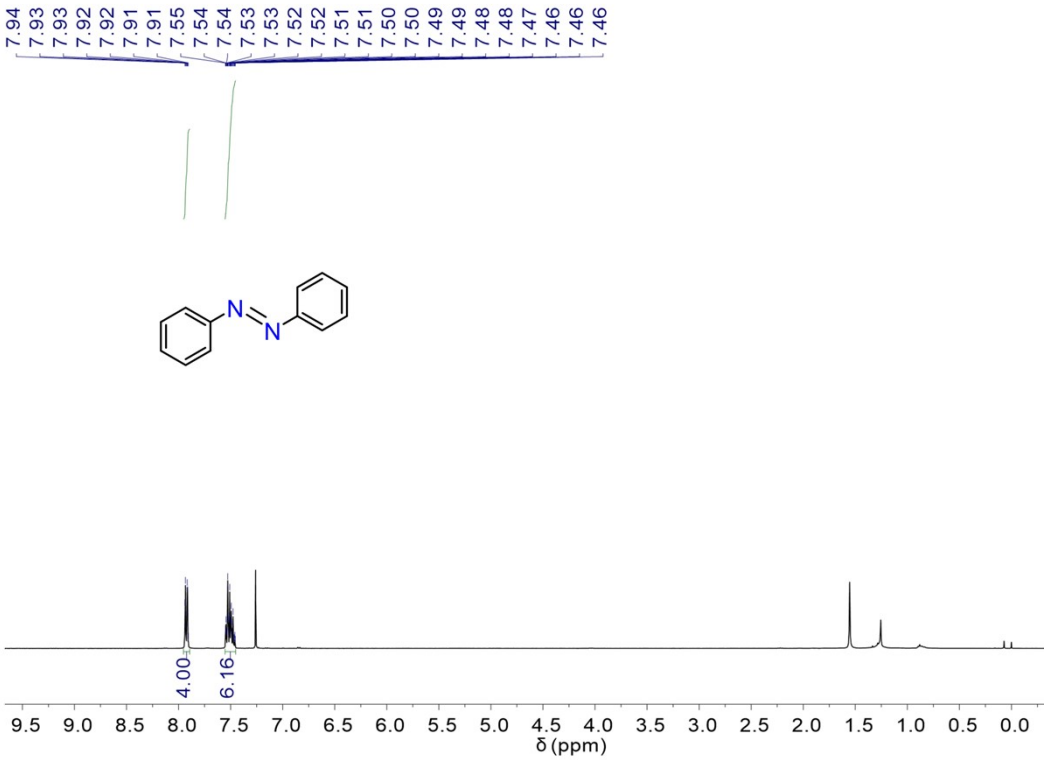

Fig. S74 ^{1}H NMR (400 MHz, $CDCl_3$, 298 K) spectrum of **3a**.

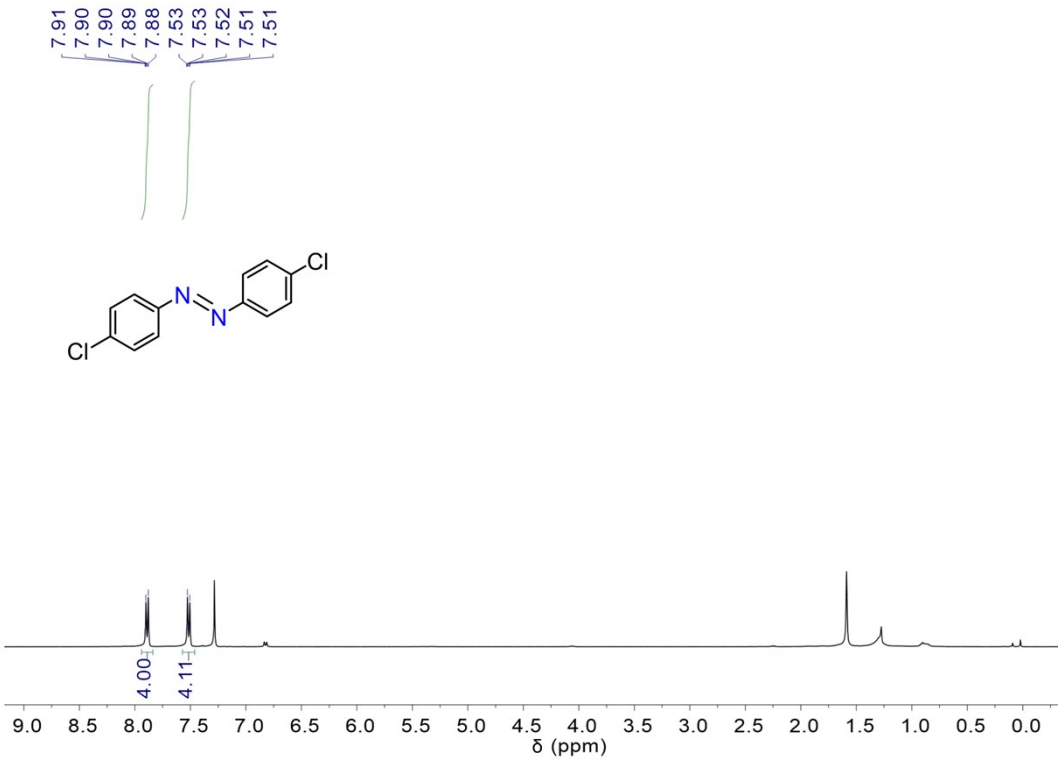

Fig. S75 ^{1}H NMR (400 MHz, $CDCl_3$, 298 K) spectrum of **3b**.

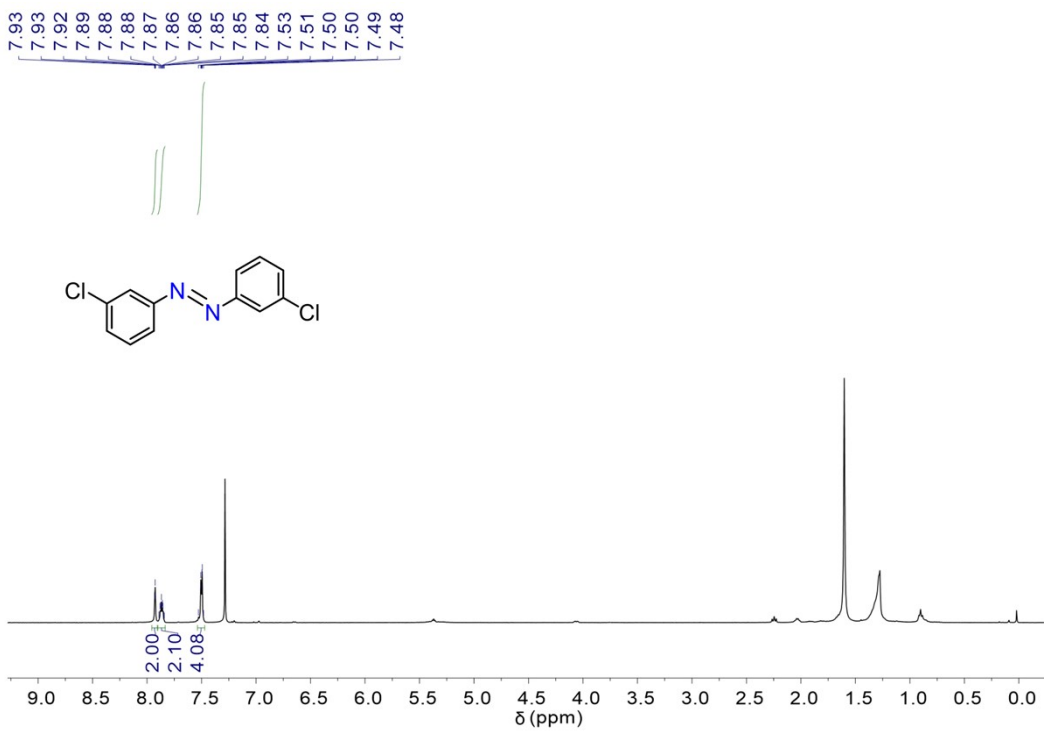

Fig. S76 ^{1}H NMR (400 MHz, $CDCl_3$, 298 K) spectrum of **3c**.

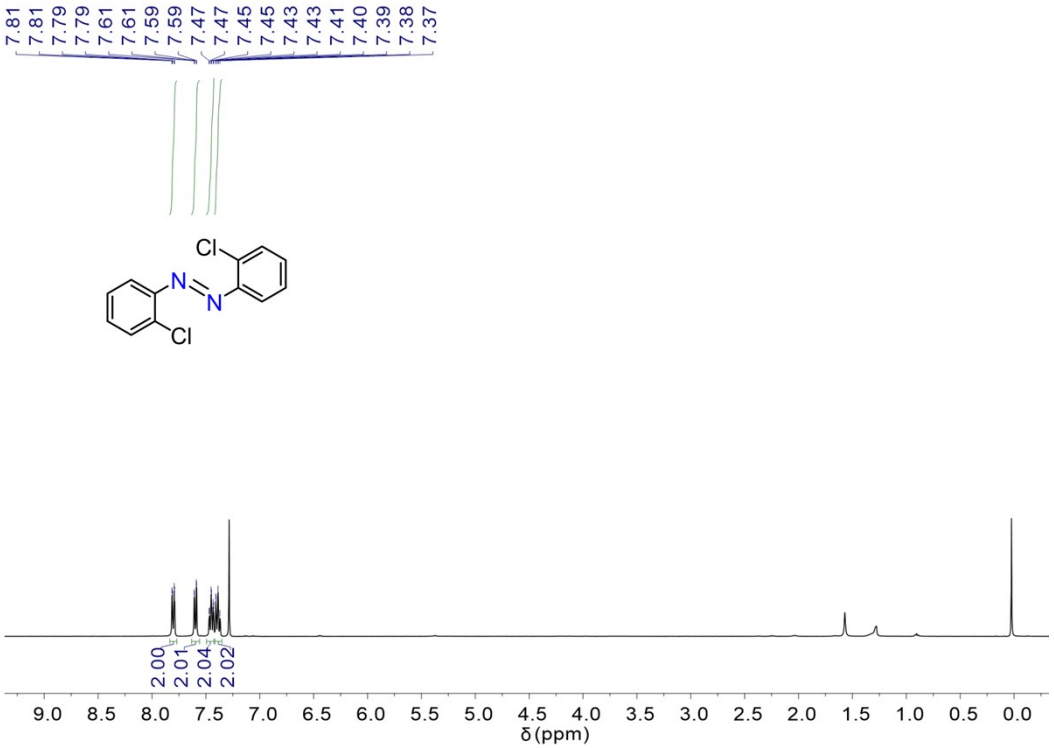

Fig. S77 ^{1}H NMR (400 MHz, $CDCl_3$, 298 K) spectrum of **3d**.

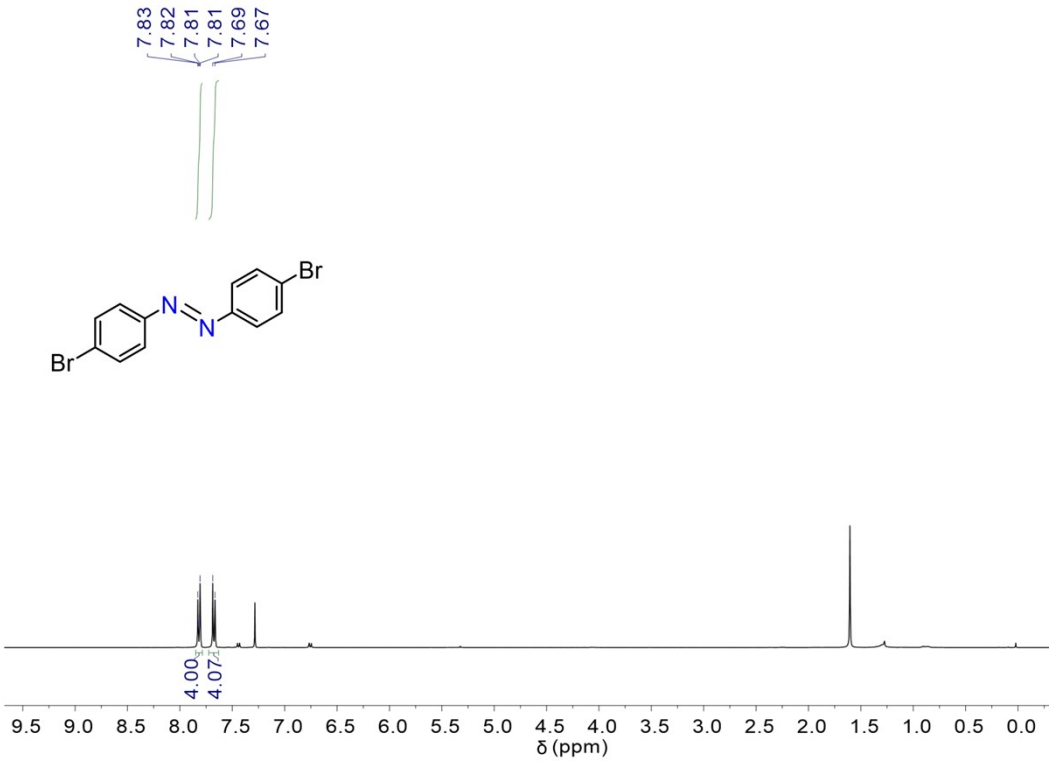

Fig. S78 ^{1}H NMR (400 MHz, $CDCl_3$, 298 K) spectrum of **3e**.

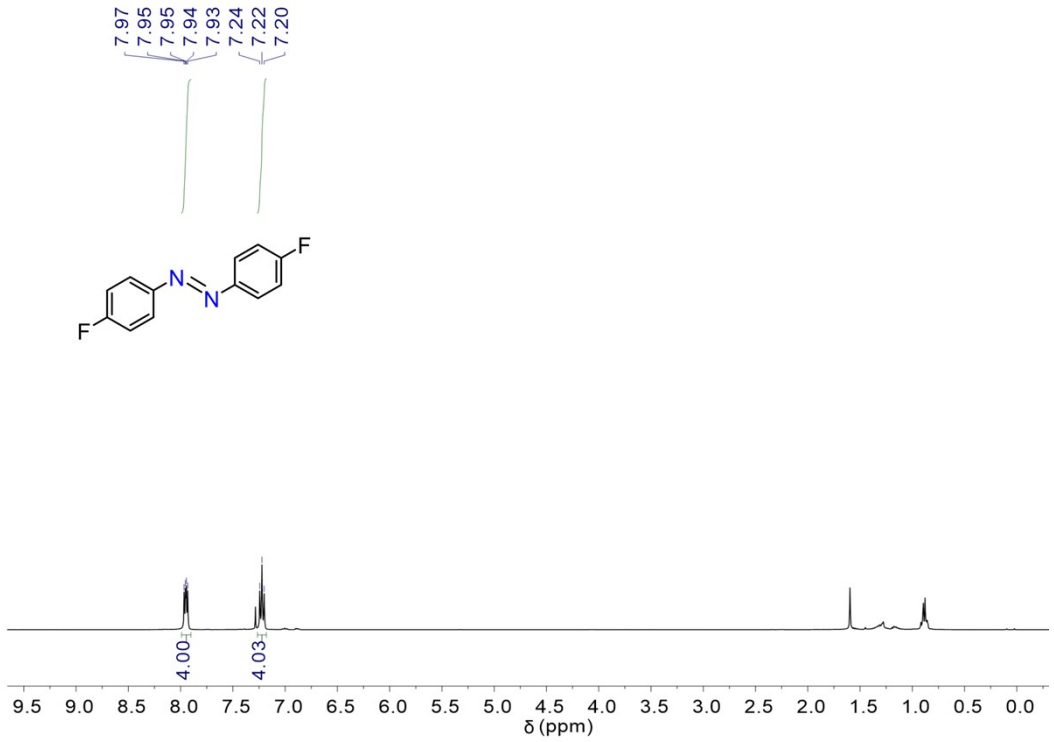

Fig. S79 ^{1}H NMR (400 MHz, $CDCl_3$, 298 K) spectrum of **3f**.

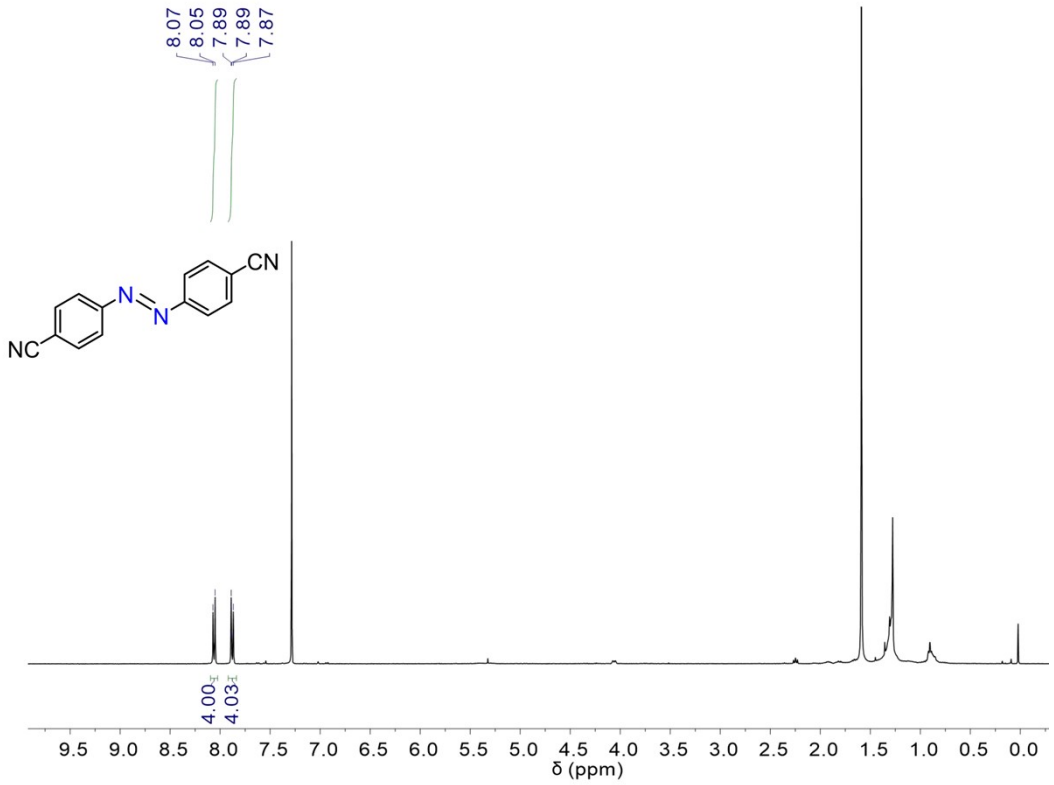

Fig. S80 ^{1}H NMR (400 MHz, $CDCl_3$, 298 K) spectrum of **3g**.

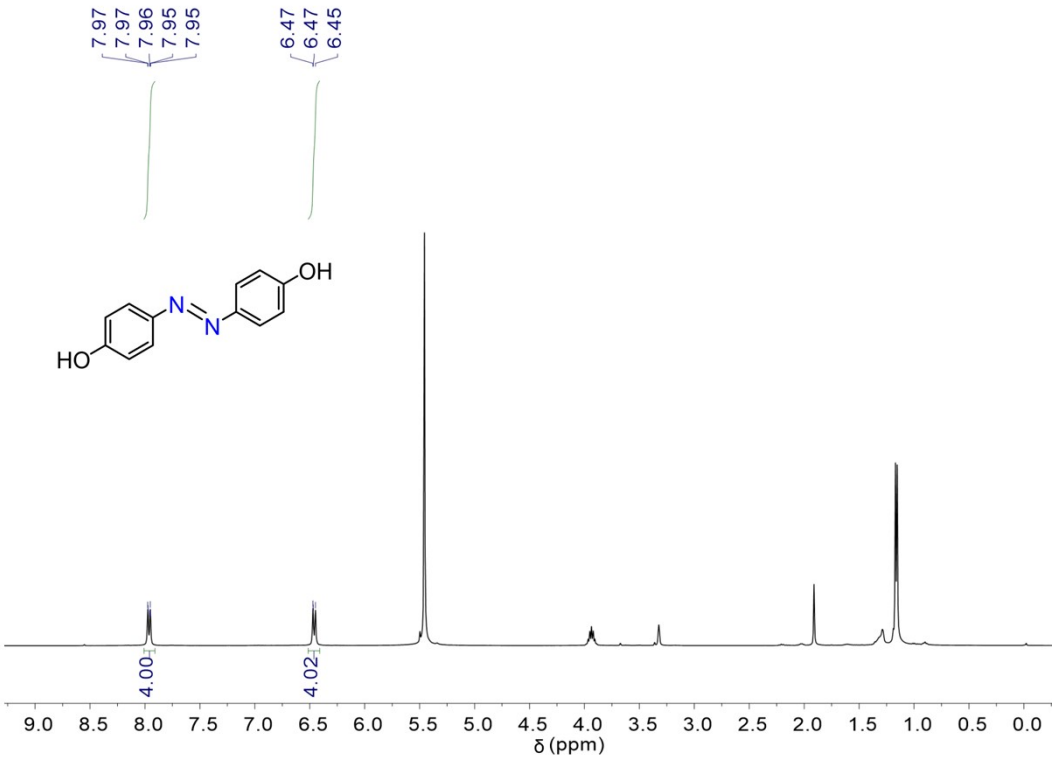

Fig. S81 ^{1}H NMR (400 MHz, CD_3OD, 298 K) spectrum of **3h**.

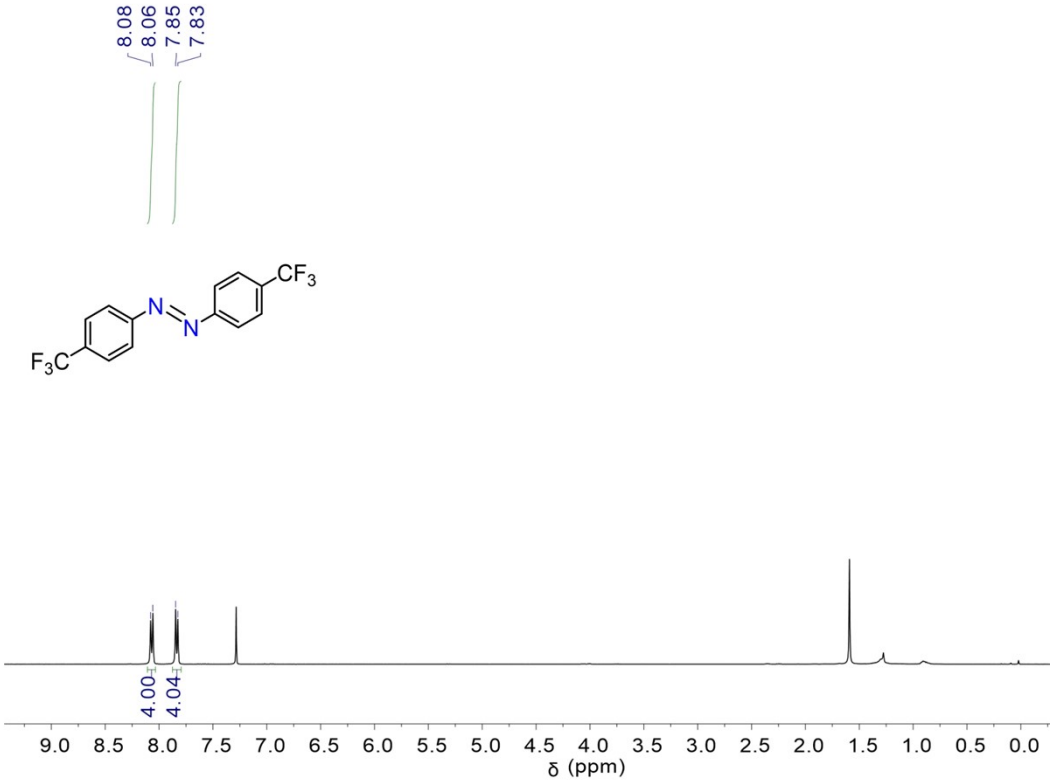

Fig. S82 ^{1}H NMR (400 MHz, $CDCl_3$, 298 K) spectrum of **3i**.

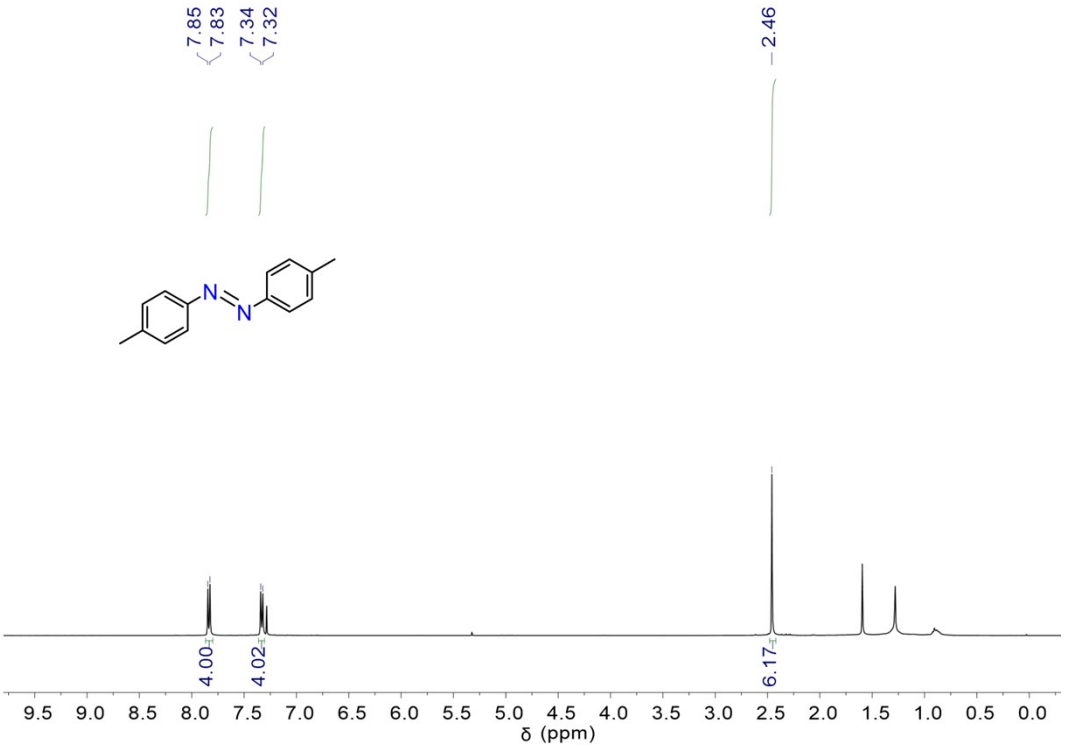

Fig. S83 ^{1}H NMR (400 MHz, $CDCl_3$, 298 K) spectrum of **3j**.

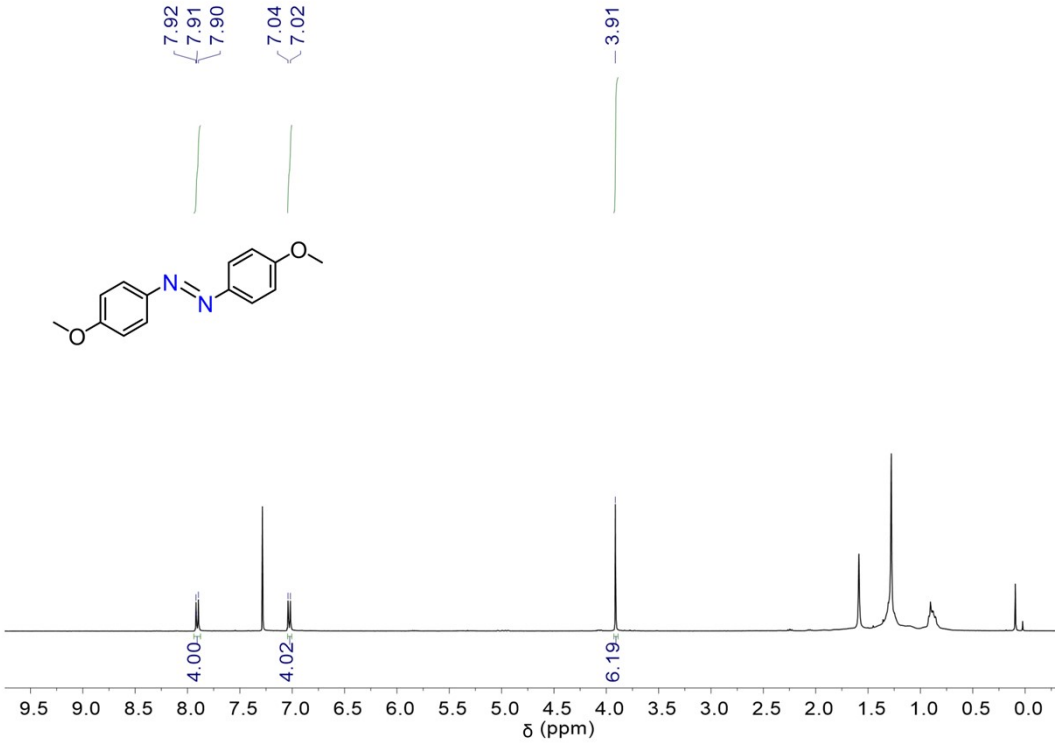

Fig. S84 ^{1}H NMR (400 MHz, $CDCl_3$, 298 K) spectrum of **3k**.

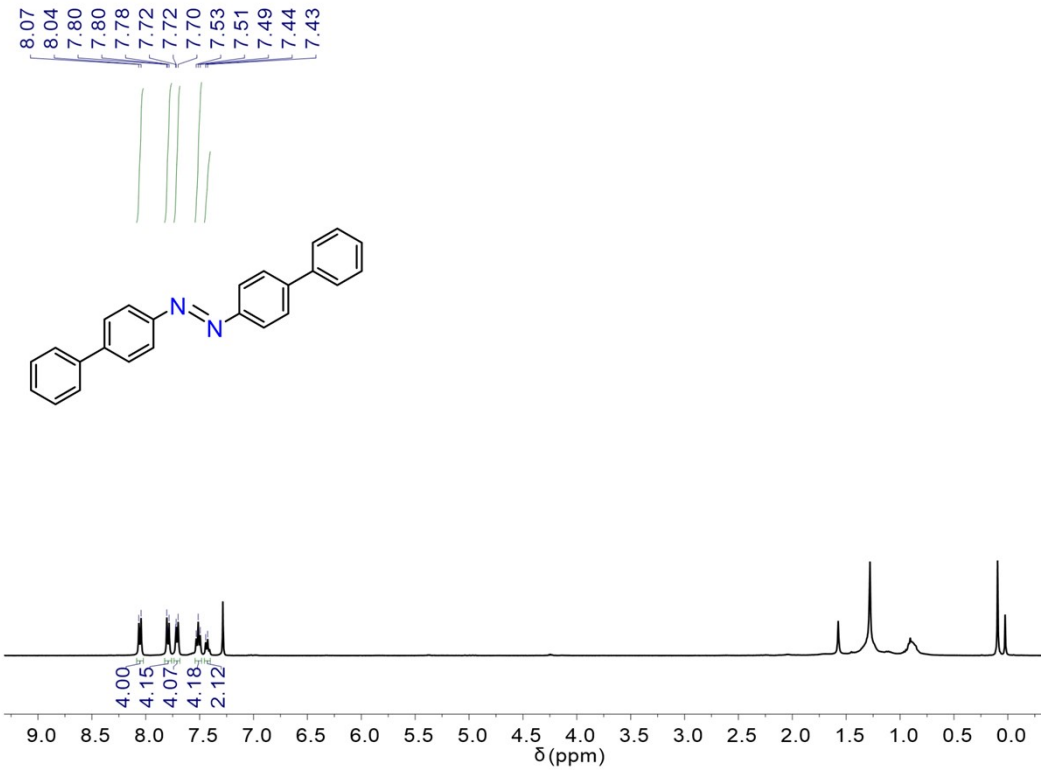

Fig. S85 ^{1}H NMR (400 MHz, $CDCl_3$, 298 K) spectrum of **3l**.

Section 8. References

[S1] P. Thordarson, Determining association constants from titration experiments in supramolecular chemistry, *Chem. Soc. Rev.*, 2011, **40**, 1305-1323.

[S2] M. R. Eftink, in *Topics in Fluorescence Spectroscopy: Principles*, ed. J. R. Lakowicz, Fluorescence Quenching: Theory and Applications, Springer US, Boston, MA, 2002, 53-126.

[S3] A. D. Becke, Density-functional thermochemistry. V. Systematic optimization of exchange-correlation functionals, *J. Chem. Phys.* **1997**, *107* (20), 8554-8560.

[S4] S. Grimme, Semiempirical GGA-type density functional constructed with a long-range dispersion correction, *J. Comput. Chem.* **2006**, *27* (15), 1787-1799.

[S5] P. J. Hay, W. R. Wadt, Ab initio effective core potentials for molecular calculations. Potentials for K to Au including the outermost core orbitals, *J. Chem. Phys.* **1985**, 82 (1), 270-283.

[S6] G. A. Petersson, A. Bennett, T. G. Tensfeldt, M. A. Al-Laham, W. A. Shirley, J. A. Mantzaris, The total energies of closed-shell atoms and hydrides of the first-row elements, *J. Chem. Phys.* **1988**, *89* (4), 2193-2218.

[S7] Gaussian 16, Revision B.01, M. J. Frisch, G. W. Trucks, H. B. Schlegel, G. E. Scuseria, M. A. Robb, J. R. Cheeseman, G. Scalmani, V. Barone, G. A. Petersson, H. Nakatsuji, X. Li, M. Caricato, A. V. Marenich, J. Bloino, B. G. Janesko, R. Gomperts, B. Mennucci, H. P. Hratchian, J. V. Ortiz, A. F. Izmaylov, J. L. Sonnenberg, D. Williams-Young, F. Ding, F. Lipparini, F. Egidi, J. Goings, B. Peng, A. Petrone, T. Henderson, D. Ranasinghe, V. G. Zakrzewski, J. Gao, N. Rega, G. Zheng, W. Liang, M. Hada, M. Ehara, K. Toyota, R. Fukuda, J. Hasegawa, M. Ishida, T. Nakajima, Y. Honda, O. Kitao, H. Nakai, T. Vreven, K. Throssell, J. A. Montgomery, J. E. Peralta, F. Ogliaro, M. J. Bearpark, J. J. Heyd, E. N. Brothers, K. N. Kudin, V. N. Staroverov, T. A. Keith, R. Kobayashi, J. Normand, K. Raghavachari, A. P. Rendell, J. C. Burant, S. S. Iyengar, J. Tomasi, M. Cossi, J. M. Millam, M. Klene, C. Adamo, R. Cammi, J. W. Ochterski, et.al., Gaussian, Inc., Wallingford CT, 2016.

[S8] T. Lu, F. Chen, Multiwfn: A multifunctional wavefunction analyzer, *J. Comput. Chem.* **2012**, 33, 580-592.

[S9] T. Lu, A comprehensive electron wavefunction analysis toolbox for chemists, Multiwfn, *J. Chem. Phys.* **2024**, 161 (8), 082503.

[S10] Z. Liu, T. Lu, Q. Chen, An sp-hybridized all-carboatomic ring, cyclo[18]carbon: Electronic structure, electronic spectrum, and optical nonlinearity, *Carbon* **2020**, *165*, 461-467.

[S11] W. Humphrey, A. Dalke, K. Schulten, VMD: Visual molecular dynamics, *J. Mol. Graph.* **1996**, 14, 33-38.

[S12] J. Wu, X. Li, P. Wu, Z. Shi, L. Chen, R. Zhang, C. He, C. Duan, Engineering Homochiral Dinuclear Ir(III)-Metallohelix-Based Porous Molecular Crystals for Atropisomer Enantioseparation, *Chem. Mater.* **2022**, *34*, 4471-4478.